Variationally consistent homogenization of electrochemical ion transport in a porous structural battery electrolyte

(article starts on next page)

Variationally consistent homogenization of electrochemical ion transport in a porous structural battery electrolyte

Vinh Tu [a,b,*], Fredrik Larsson [a], Kenneth Runesson [a], Ralf Jänicke [b]

[a] *Department of Industrial and Materials Science, Chalmers University of Technology, 41296, Gothenburg, Sweden*
[b] *Institute of Applied Mechanics, Technische Universität Braunschweig, 38106, Braunschweig, Germany*

ABSTRACT

In this paper, we develop a multi-scale modeling framework for a multiphysics problem characterized by electro-chemically coupled ion transport in a Structural Battery Electrolyte (SBE). The governing equations of the problem are established by coupling Gauss law with mass conservation for each mobile species. By utilizing variationally consistent homogenization, we are able to establish a two-scale model where both the macro-scale and sub-scale equations are deduced from a single-scale problem. Investigations of the sub-scale RVE problem show that the transient effects are negligible for the length scales relevant to the studied application, which motivates the assumption of micro-stationarity. In the special case of linear constitutive response, we get a numerically efficient solution scheme for the macro-scale problem that is based on a priori upscaling. As a final step, we demonstrate the numerically efficient solution scheme by solving a 2D macro-scale problem using upscaled constitutive quantities based on a 3D RVE.

1. Introduction

The structural battery is, unlike conventional monofunctional batteries, multifunctional in the sense that it is able to carry mechanical loads, and at the same time store and deliver energy (Asp and Greenhalgh, 2014; Asp et al., 2019). This is made possible by the carbon fiber's reversible lithium insertion capability (Kanno et al., 1992) and its intrinsic ability to both conduct current and carry tensile load, which has enabled the possibility to exploit carbon fibers as battery electrodes (Kjell et al., 2011; Fredi et al., 2018) as opposed to particle based electrodes used in conventional batteries. Although the carbon fibers can directly act as the negative electrodes, they need to be coated with a layer comprising lithium metal oxide or olivine based particles, e.g. $LiFePO_4$, binder and conductive additives in order to function as the positive electrodes (Hagberg et al., 2018; Moyer et al., 2020; Sanchez et al., 2021). While conventional batteries rely on electrolytes in liquid form to allow for ion transfer between the electrodes, the structural battery utilizes the so-called Structural Battery Electrolyte (SBE) (Shirshova et al., 2013; Ihrner et al., 2017; Schneider et al., 2019). The SBE consists of two continuous phases; a liquid electrolyte and a porous polymer skeleton with pore size ranging from 50 to 200 nm (Ihrner et al., 2017; Schneider et al., 2019). The role of the liquid electrolyte is to allow for ion transfer, while the porous polymer skeleton provides structural integrity. In short, each constituent of the structural battery is designed to be multifunctional and utilized

to its fullest potential, hence ensuring that significant weight and volume savings are achieved (Asp and Greenhalgh, 2014; Asp et al., 2019; Johannisson et al., 2019). However, it should be noted that the complexity of the structural battery gives rise to numerous challenges that need to be addressed.

The performance prediction for various microstructure designs of the SBE represents a major challenge (Asp and Greenhalgh, 2014; Asp et al., 2019). In order to truly optimize the design w.r.t. the multifunctional performance, further development of modeling tools is needed. In Tu et al. (2020), the mechanical and transport properties were compared numerically for a variety of experimentally studied structural electrolytes, whereby synthetically generated microstructures and simplified models were used. That is, the more elaborate electrochemical problem, involving both migration and diffusion of ions, was not considered.

Works related to modeling and simulation of electrochemical systems are abundant in the literature. Newman et al. developed the first numerical models of coupled electrochemical reaction–diffusion in batteries (Newman and Tiedemann, 1975; Doyle et al., 1993; Doyle and Newman, 1995). As to the modeling of ion transport in conventional batteries, we note the works by Samson et al. (1999), Danilov and Notten (2008), Dickinson et al. (2011), Bauer et al. (2012) to mention a few. Salvadori and co-workers formulated the governing equations

---

pertaining to the multi-scale analysis of electrochemical systems, Salvadori et al. (2014, 2015a), and performed simulations in 1D and 2D (Salvadori et al., 2015b). Interest in the modeling of the multi-physics couplings in structural batteries has emerged in recent years, e.g. Xu et al. (2018) and Carlstedt et al. (2020, 2022b,a).

In this paper, the goal is to develop a multi-scale modeling framework for electro-chemically coupled ion transport in the SBE. The governing equations are established by combining Gauss law (as opposed to the classical electro-neutrality assumption (Dickinson et al., 2011)) with mass conservation for each mobile species (Salvadori et al., 2014, 2015a,b; Wilmers et al., 2017; Griffiths et al., 2020). In the next step, the so-called Variationally Consistent Homogenization (VCH) (Larsson et al., 2010) theory is exploited. As a result, both the macro-scale and sub-scale Representative Volume Element (RVE) problems are deduced from a fine-scale (single-scale) problem with proper scale-bridging. Notably, all constitutive relations are introduced only for the sub-scale problem. The VCH concept relies on classical (model-based) homogenization, the assumption of scale separation via first-order homogenization, and scale bridging via a macro-homogeneity condition that generalizes the classical Hill–Mandel condition (Hill, 1963) such that it applies even for transient problems. Due to the exploitation of VCH in transient diffusion problems, non-standard higher order conservation quantities will appear (Larsson et al., 2010; Jänicke et al., 2020). While special care must be taken when dealing with dynamic problems (e.g. mechanical problems with dynamic and inertia effects), it should be noted here that first order homogenization is known to work well for parabolic problems such as transient diffusion (Polukhov and Keip, 2020; Kaessmair and Steinmann, 2018).

Among the numerous applications of VCH in the literature, we mention Stokes' flow (Sandstrom and Larsson, 2013), coupled flow and deformation in a porous material (Su et al., 2011; Sandström et al., 2016), liquid-phase sintering (Öhman et al., 2013), and phase-field fracture (Bharali et al., 2021). However, none of the above-mentioned works deal with electro-chemically coupled transient transport of electroactive species in porous (bicontinuous) materials. Although the present paper concerns application to the structural battery, the proposed multi-scale modeling framework is sufficiently general to cover homogenization of electrochemical systems in porous materials. Examples of other applications are structural supercapacitors (Shirshova et al., 2013) and separator membranes in conventional battery applications (Costa et al., 2019).

The remainder of the paper is structured as follows: Governing equations and constitutive relations are established for the fine-scale problem in Section 2. Based on the fine-scale model, the corresponding macro-scale and sub-scale problems are deduced via VCH in Section 3. A 2D RVE study and numerical validation of the two-scale approximation versus a fully resolved reference problem is performed in Section 4. Finally, the paper concludes with computational results for a 2D macro-scale problem based on upscaled constitutive quantities from a 3D RVE.

2. Fine-scale modeling

In this section, we start off by defining the governing equations that describe the electro-chemically coupled transient transport of electroactive species in the SBE. This is achieved by combining Gauss law in differential form with mass conservation for mobile species. In the next step, we define the relevant constitutive relations in the liquid electrolyte domain Ω_E and solid polymer domain Ω_S. Although all ion related equations are formulated in a general format for any number of ions $\alpha = 1, 2, \ldots, N$, the electrochemical system considered in the numerical simulations will consist of Li$^+$ and a corresponding companion anion (e.g. PF$_6^-$) that we will simply denote X$^-$.
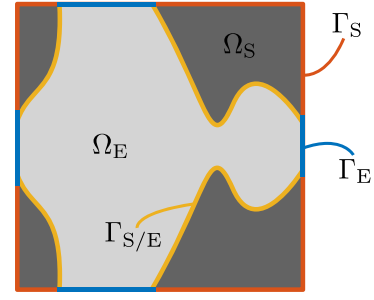

Fig. 1. SBE consists of solid and electrolyte domains, i.e. $\Omega = \Omega_S \cup \Omega_E$. External boundary of the SBE is decomposed as $\partial\Omega = \Gamma_S \cup \Gamma_E = \Gamma_D^{(\varphi)} \cup \Gamma_N^{(\varphi)}$, and the boundary surrounding the electrolyte domain is decomposed as $\partial\Omega_E = \Gamma_E \cup \Gamma_{S/E} = \Gamma_{D,\alpha}^{(\mu)} \cup \Gamma_{N,\alpha}^{(\mu)} \cup \Gamma_{S/E}$.

2.1. Balance equations for the fine-scale problem

Restricting to electrostatics, we seek the electric potential $\varphi(\boldsymbol{x}, t)$: $\Omega \times \mathbb{R}^+ \to \mathbb{R}$ and the chemical potentials $\mu_\alpha(\boldsymbol{x}, t)$: $\Omega_E \times \mathbb{R}^+ \to \mathbb{R}$, $\alpha = 1, 2, \ldots, N$, that solve the system

$$\rho - \boldsymbol{d} \cdot \boldsymbol{\nabla} = 0 \quad \text{in } \Omega \times (0, T], \tag{1a}$$

$$\partial_t c_\alpha + \boldsymbol{j}_\alpha \cdot \boldsymbol{\nabla} = 0 \quad \text{in } \Omega_E \times (0, T], \tag{1b}$$

$$\varphi = \varphi^p \quad \text{on } \Gamma_D^{(\varphi)} \times (0, T], \tag{1c}$$

$$d := \boldsymbol{d} \cdot \boldsymbol{n} = d^p \quad \text{on } \Gamma_N^{(\varphi)} \times (0, T], \tag{1d}$$

$$\mu_\alpha = \mu_\alpha^p \quad \text{on } \Gamma_{D,\alpha}^{(\mu)} \times (0, T], \tag{1e}$$

$$j_\alpha := \boldsymbol{j}_\alpha \cdot \boldsymbol{n} = j_\alpha^p \quad \text{on } \Gamma_{N,\alpha}^{(\mu)} \times (0, T], \tag{1f}$$

$$j_\alpha = 0 \quad \text{on } \Gamma_{S/E} \times (0, T], \tag{1g}$$

together with suitably defined constitutive relations and the initial condition

$$c_\alpha(\bullet, 0) = c_{\alpha,0} \quad \text{in } \Omega_E, \tag{2}$$

see Fig. 1 for the domain and boundary decompositions.

Eq. (1a) represents Gauss law, where ρ and $\boldsymbol{d}$ are the volume charge density per unit volume and the electric flux density (electric displacement field), respectively. The equation is valid in the entire domain $\Omega = \Omega_S \cup \Omega_E$ and the boundary conditions are exemplified on $\partial\Omega = \Gamma_D^{(\varphi)} \cup \Gamma_N^{(\varphi)}$ in terms of Dirichlet (1c) and Neumann conditions (1d).

Eq. (1b) expresses the conservation of species α in terms of the volume specific molar concentration c_α and the molar (ionic) flux $\boldsymbol{j}_\alpha$. This equation is valid only in the electrolyte domain Ω_E, where the boundary is decomposed as $\partial\Omega_E = \Gamma_{D,\alpha}^{(\mu)} \cup \Gamma_{N,\alpha}^{(\mu)} \cup \Gamma_{S/E}$ for each species α. In other words, there is no transport of ionic species in the solid domain Ω_s. Eq. (1g) expresses the inability of the species to enter the solid domain on the solid-electrolyte interface $\Gamma_{S/E} = \partial\Omega_S \cap \partial\Omega_E$, while Eq. (1e) and (1f) exemplify the external boundary conditions of Dirichlet and Neumann type respectively.

2.2. Constitutive relations of the fine-scale model

The constitutive relations for the electric flux density $\boldsymbol{d}$ and the ionic flux $\boldsymbol{j}_\alpha$ are introduced as follows

$$\boldsymbol{d} := \boldsymbol{\epsilon} \cdot \boldsymbol{e}, \quad \boldsymbol{e}[\varphi] := -\boldsymbol{\nabla}\varphi, \tag{3a}$$

$$\boldsymbol{j}_\alpha := -\boldsymbol{M}_\alpha \cdot [\boldsymbol{\nabla}\mu_\alpha + z_\alpha' \boldsymbol{\nabla}\varphi], \tag{3b}$$

where φ is the electric potential and μ_α the chemical potential of a mobile species ($\alpha = 1, 2, \ldots, N$) with the ionic charge $z_\alpha' = F z_\alpha$. Here, F corresponds to the Faraday constant and z_α is the valance of species α. The material properties are given as the electric permittivity $\boldsymbol{\epsilon}$ and the ionic mobility $\boldsymbol{M}_\alpha$ of species α. Both quantities are second rank

tensors that can, in the simple case of material isotropy, be condensed to the scalar electric permittivity ϵ and ionic mobility M_α.

Furthermore, the volume charge density ρ (charge per unit volume) and the molar concentration c_α of species α are defined as

$$\rho := \begin{cases} \sum_{\alpha=1}^{N} z'_\alpha c_\alpha & \text{in } \Omega_{\mathrm{E}}, \\ 0 & \text{in } \Omega_{\mathrm{S}}, \end{cases} \tag{4a}$$

$$c_\alpha := c_\alpha(\{\mu_\beta\}_{\beta=1}^{N}) \quad \text{in } \Omega_{\mathrm{E}}. \tag{4b}$$

The molar concentration c_α quantifies the number of ions of species α stored in the material point. Assuming, for convenience, a dilute distribution of charged ions in the electrolyte and neglecting ion interactions between different species, the concentration c_α of each species can be computed from the chemical potential μ_α via the relation

$$\mu_\alpha = \mu_{\alpha,0} + RT \ln\left(\gamma_\alpha(c_\alpha)\, c_\alpha\right), \tag{5}$$

where $\mu_{\alpha,0}$ is the reference chemical potential of species α, R the gas constant, T the temperature and $\gamma_\alpha = \gamma_\alpha(c_\alpha)$ the activity coefficient of species α. Moreover, if the chemical potential changes are assumed to be small around the concentration level $c_\alpha = c_{\alpha,0}$, then relation (5) can be linearized. Linearization of (5) around $c_\alpha = c_{\alpha,0}$ and assuming $\mu_{\alpha,0} = -RT \ln\left(\gamma_\alpha(c_{\alpha,0})\, c_{\alpha,0}\right)$ results in the relation

$$c_\alpha = k_\alpha \mu_\alpha + c_{\alpha,0}, \tag{6}$$

where k_α depends on the choice of $\gamma_\alpha(c_\alpha)$. In the subsequent analysis, we choose γ_α constant, which results in $k_\alpha = \frac{c_{\alpha,0}}{RT}$.

Finally, the (ionic) current density in the electrochemical system can be computed via Faraday's rule of electrolysis as a post-processed quantity in the following fashion

$$\boldsymbol{i} := \sum_{\alpha=1}^{N} z'_\alpha \boldsymbol{j}_\alpha. \tag{7}$$

2.3. Weak format of the fine-scale problem

The standard space-variational format corresponding to (1) reads: Find $\varphi(\bullet,t), \{\mu_\alpha(\bullet,t)\}$ in the appropriately defined spaces $\mathbb{P} \times \{\mathbb{M}_\alpha\}_{\alpha=1}^{N}$ that solve

$$\int_\Omega \delta\varphi\, \rho\, \mathrm{d}\Omega + \int_\Omega \boldsymbol{\nabla}\delta\varphi \cdot \boldsymbol{d}\, \mathrm{d}\Omega = \int_{\Gamma_{\mathrm{N}}^{(\varphi)}} \delta\varphi\, d^{\mathrm{p}}\, \mathrm{d}\Gamma \quad \forall \delta\varphi \in \mathbb{P}^0, \tag{8a}$$

$$\int_{\Omega_{\mathrm{E}}} \delta\mu_\alpha\, \partial_t c_\alpha\, \mathrm{d}\Omega - \int_{\Omega_{\mathrm{E}}} \boldsymbol{\nabla}\delta\mu_\alpha \cdot \boldsymbol{j}_\alpha\, \mathrm{d}\Omega = -\int_{\Gamma_{\mathrm{N}}^{(\alpha)}} \delta\mu_\alpha\, j_\alpha^{\mathrm{p}}\, \mathrm{d}\Gamma \quad \forall \delta\mu_\alpha \in \mathbb{M}_\alpha^0, \tag{8b}$$

$\alpha = 1, 2, \ldots, N$, where $\mathbb{P}^0$ and $\{\mathbb{M}_\alpha^0\}_{\alpha=1}^{N}$ are the appropriately defined test spaces. Initial conditions are appropriately defined.

3. Two-scale analysis based on computational homogenization

By accounting for the SBE microstructure features, it becomes computationally infeasible to solve the single-scale model due to the length scale difference. Therefore, we utilize a two-scale modeling approach where a smooth macro-scale problem and a sub-scale RVE problem is derived from the single scale model via VCH (Larsson et al., 2010).

3.1. First order homogenization in the spatial domain

We replace the single-scale problem in Section 2 by a two-scale problem upon introducing (i) running averages in the weak format and (ii) scale separation via first-order homogenization. The first step is to replace the space-variational problem in (8) by that of finding $(\varphi(\bullet,t), \{\mu_\alpha(\bullet,t)\}) \in \mathbb{P}_{\mathrm{FE}^2} \times \{\mathbb{M}_{\alpha,\mathrm{FE}^2}\}_{\alpha=1}^{N}$ that solves
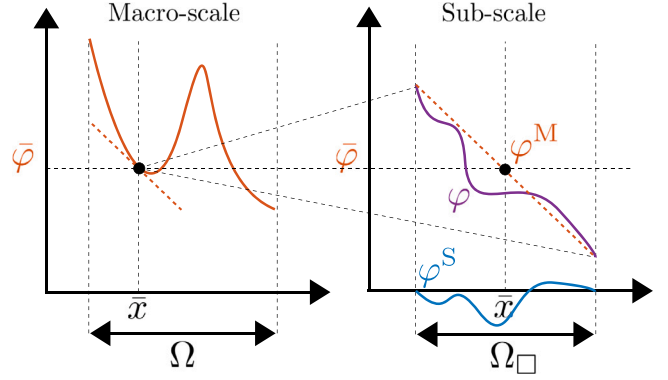

Fig. 2. Illustration on the prolongation of electric potential. Fully resolved sub-scale field constructed by using information from the smooth macro-scale solution.

$$\int_\Omega \left[\langle \delta\varphi\, \rho \rangle_\square + \langle \boldsymbol{\nabla}\delta\varphi \cdot \boldsymbol{d} \rangle_\square \right] \mathrm{d}\Omega = \int_{\Gamma_{\mathrm{N}}^{(\varphi)}} \delta\varphi\, d^{\mathrm{p}}\, \mathrm{d}\Gamma$$
$$\forall \delta\varphi \in \mathbb{P}_{\mathrm{FE}^2}^0, \tag{9a}$$

$$\int_\Omega \left[\phi\, \langle \delta\mu_\alpha\, \partial_t c_\alpha \rangle_{\square,\mathrm{E}} - \phi\, \langle \boldsymbol{\nabla}\delta\mu_\alpha \cdot \boldsymbol{j}_\alpha \rangle_{\square,\mathrm{E}} \right] \mathrm{d}\Omega = -\int_{\Gamma_{\mathrm{N},\alpha}^{(\mu)}} \delta\mu_\alpha\, j_\alpha^{\mathrm{p}}\, \mathrm{d}\Gamma$$
$$\forall \delta\mu_\alpha \in \mathbb{M}_{\alpha,\mathrm{FE}^2}^0, \tag{9b}$$

where the initial conditions are appropriately defined. Here, the pertinent volume averaging operators and porosity in (9) are defined as

$$\langle \bullet \rangle_\square := \frac{1}{|\Omega_\square|} \int_{\Omega_\square} \bullet\, \mathrm{d}\Omega, \tag{10a}$$

$$\langle \bullet \rangle_{\square,\mathrm{E}} := \frac{1}{|\Omega_{\square,\mathrm{E}}|} \int_{\Omega_{\square,\mathrm{E}}} \bullet\, \mathrm{d}\Omega, \tag{10b}$$

$$\phi := \frac{|\Omega_{\square,\mathrm{E}}|}{|\Omega_\square|}. \tag{10c}$$

The volume averaged integrands in (9) represent running averages on square/cubic domains $\Omega_\square$ with the side length $L_\square$ and are centered at each macro-scale spatial point $\bar{\boldsymbol{x}} \in \Omega$. Note that the introduction of running averages results in a change of the original problem. The weak format (9) will thus serve as the basis for VCH, which is elaborated upon in the next step. (see Fig. 2). In order to define the two-scale solution and test spaces[1] $\mathbb{P}_{\mathrm{FE}^2}, \mathbb{M}_{\alpha,\mathrm{FE}^2}$ and $\mathbb{P}_{\mathrm{FE}^2}^0, \mathbb{M}_{\alpha,\mathrm{FE}^2}^0$ associated with Finite Element squared (FE²), we introduce scale separation and first-order homogenization. We refer to FE² in a discrete sense, where $\Omega_{\square,i}$ pertains to an RVE centered at the macro-scale quadrature point $\bar{\boldsymbol{x}}_i$. Note that an FE² approach is unnecessary for stationary problems with linear constitutive relations, however, the two-scale problem presented in this section is in fact linear transient. In other words, each RVE would still need to resolve the transient effects at each macroscopic quadrature point, which would warrant solving the two-scale problem using a FE² approach.

The standard prolongation approach is to decompose the sub-scale fields φ and μ_α into macro-scale parts, φ^{M} and μ_α^{M}, and micro-scale (fluctuating) parts, φ^{S} and μ_α^{S}, within each RVE such that

$$\varphi = \varphi^{\mathrm{M}}[\bar{\varphi}] + \varphi^{\mathrm{S}}, \quad \varphi^{\mathrm{M}}[\bar{\varphi}](\bar{\boldsymbol{x}}; \boldsymbol{x}, t) := \bar{\varphi}(\bar{\boldsymbol{x}}, t) + \bar{\boldsymbol{g}}^\varphi[\bar{\varphi}](\bar{\boldsymbol{x}}, t) \cdot [\boldsymbol{x} - \bar{\boldsymbol{x}}],$$
$$\bar{\boldsymbol{g}}^\varphi := \boldsymbol{\nabla}\bar{\varphi}, \tag{11a}$$

---

[1] Here, we use the notation FE² alluding to the numerical formulation of the problem, even though we have not discussed the finite element discretization.

$$\mu_\alpha = \mu_\alpha^M[\bar\mu_\alpha] + \mu_\alpha^S, \quad \mu_\alpha^M[\bar\mu_\alpha](\bar{\boldsymbol{x}};\boldsymbol{x},t) := \bar\mu_\alpha(\bar{\boldsymbol{x}},t) + \bar{\boldsymbol{g}}_\alpha^\mu[\bar\mu_\alpha](\bar{\boldsymbol{x}},t) \cdot [\boldsymbol{x} - \bar{\boldsymbol{x}}],$$

$$\bar{\boldsymbol{g}}_\alpha^\mu := \boldsymbol{\nabla}\bar\mu_\alpha, \tag{11b}$$

for $\alpha = 1, 2, \ldots, N$, see Fig. 2 for an illustration on the prolongation rule. Note that we introduced the homogenized fields $\bar\varphi(\bar{\boldsymbol{x}},t)$ and $\bar\mu_\alpha(\bar{\boldsymbol{x}},t)$ that correspond to the smooth macro-scale solutions. They are used here to define the macroscopic components of the Taylor expansions. Conversely, we define $\bar\varphi$ and its gradient $\bar{\boldsymbol{g}}^\varphi$ through homogenization operators as

$$\bar\varphi = \bar\varphi_\square(\varphi), \quad \bar\varphi_\square(\varphi) := \langle\varphi\rangle_\square, \tag{12a}$$

$$\bar{\boldsymbol{g}}^\varphi = \bar{\boldsymbol{g}}_\square^\varphi(\varphi), \quad \bar{\boldsymbol{g}}_\square^\varphi(\varphi) := \langle\boldsymbol{\nabla}\varphi\rangle_\square. \tag{12b}$$

By construction of the operators, the relations $\bar\varphi_\square(\varphi^M) = \bar\varphi$ and $\bar{\boldsymbol{g}}_\square^\varphi(\varphi^M) = \bar{\boldsymbol{g}}^\varphi$ will be satisfied when the prolongation defined in (11) is exploited. Due to linearity, the relations

$$\bar\varphi_\square(\varphi^S) = 0, \tag{13a}$$

$$\bar{\boldsymbol{g}}_\square^\varphi(\varphi^S) = \mathbf{0}, \tag{13b}$$

are equivalently satisfied. Analogously, the corresponding homogenization operators for $\bar\mu_\alpha$ and its gradient $\bar{\boldsymbol{g}}_\alpha^\mu$ are defined as

$$\bar\mu_\alpha = \bar\mu_{\square,\alpha}(\mu_\alpha), \quad \bar\mu_{\square,\alpha}(\mu_\alpha) := \langle\mu_\alpha\rangle_{\square,E} - \bar{\boldsymbol{g}}_{\square,\alpha}^\mu(\mu_\alpha) \cdot [\bar{\boldsymbol{x}}_E - \bar{\boldsymbol{x}}], \tag{14a}$$

$$\bar{\boldsymbol{x}}_E := \langle\boldsymbol{x}\rangle_{\square,E}, \tag{14b}$$

$$\bar{\boldsymbol{g}}_\alpha^\mu = \bar{\boldsymbol{g}}_{\square,\alpha}^\mu(\mu_\alpha), \quad \bar{\boldsymbol{g}}_{\square,\alpha}^\mu(\mu_\alpha) := \frac{1}{|\Omega_\square|} \int_{\Gamma_{\square,E}} \mu_\alpha \, \boldsymbol{n} \, d\Gamma \cdot \boldsymbol{I}_{\square,E}^{-1}, \tag{14c}$$

$$\boldsymbol{I}_{\square,E} := \frac{1}{|\Omega_\square|} \int_{\Gamma_{\square,E}} \boldsymbol{x} \otimes \boldsymbol{n} \, d\Gamma. \tag{14d}$$

Here, (14b) and (14d) take into account that the center of mass $\bar{\boldsymbol{x}}_E$ of Ω_E is in general not identical to the RVE center $\bar{\boldsymbol{x}}$. Once again, by construction of the operators, the relations $\bar\mu_{\square,\alpha}(\mu_\alpha^M) = \bar\mu_\alpha$ and $\bar{\boldsymbol{g}}_{\square,\alpha}^\mu(\mu_\alpha^M) = \bar{\boldsymbol{g}}_\alpha^\mu$ will be satisfied when the prolongation defined in (11) is exploited. Indeed, this property is the rationale for the non-standard definitions in (14). Due to linearity, the relations

$$\bar\mu_{\square,\alpha}(\mu_\alpha^S) = 0, \tag{15a}$$

$$\bar{\boldsymbol{g}}_{\square,\alpha}^\mu(\mu_\alpha^S) = \mathbf{0}, \tag{15b}$$

are equivalently satisfied.

We are now in the position to define the two-scale trial and test spaces

$$\mathbb{P}_{FE^2} := \{\varphi|_{\Omega_{\square,i}} = \varphi^M[\bar\varphi] + \varphi_i^S, \ \varphi_i^S \in \mathbb{P}_{\square,i}^S, \ \varphi|_{\Gamma_N^{(\varphi)}} = \bar\varphi, \ \bar\varphi \in \bar{\mathbb{P}}\}, \tag{16a}$$

$$\mathbb{P}_{FE^2}^0 := \{\delta\varphi|_{\Omega_{\square,i}} = \varphi^M[\delta\bar\varphi] + \delta\varphi_i^S, \ \delta\varphi_i^S \in \mathbb{P}_{\square,i}^S, \ \delta\varphi|_{\Gamma_N^{(\varphi)}} = \delta\bar\varphi, \ \delta\bar\varphi \in \bar{\mathbb{P}}^0\}, \tag{16b}$$

and for all $\alpha = 1, 2, \ldots, N$,

$$\mathbb{M}_{\alpha,FE^2} := \{\mu_\alpha|_{\Omega_{\square,i}} = \mu_\alpha^M[\bar\mu_\alpha] + \mu_{\alpha,i}^S, \ \mu_{\alpha,i}^S \in \mathbb{M}_{\square,i,\alpha}^S,$$
$$\mu_\alpha|_{\Gamma_{\alpha,N}^{(\mu)}} = \bar\mu_\alpha, \ \bar\mu_\alpha \in \bar{\mathbb{M}}_\alpha\}, \tag{17a}$$

$$\mathbb{M}_{\alpha,FE^2}^0 := \{\delta\mu_\alpha|_{\Omega_{\square,i}} = \mu_\alpha^M[\delta\bar\mu_\alpha] + \delta\mu_{\alpha,i}^S, \ \delta\mu_{\alpha,i}^S \in \mathbb{M}_{\square,i,\alpha}^S,$$
$$\delta\mu_\alpha|_{\Gamma_{\alpha,N}^{(\mu)}} = \delta\bar\mu_\alpha, \ \delta\bar\mu_\alpha \in \bar{\mathbb{M}}_\alpha^0\}. \tag{17b}$$

The trial and test spaces for the macro-scale problem are denoted $\bar{\mathbb{P}}, \bar{\mathbb{P}}^0$ and $\bar{\mathbb{M}}_\alpha, \bar{\mathbb{M}}_\alpha^0$ and for the micro-scale problem $\mathbb{P}_{\square,i}^S$, and $\mathbb{M}_{\square,i,\alpha}^S$. We introduce the notation

$$\varphi \in \mathbb{P}_{FE^2} \longrightarrow (\bar\varphi, \{\varphi_i^S\}) \in \bar{\mathbb{P}} \times \left[\times_i \mathbb{P}_{\square,i}^S\right], \tag{18a}$$

$$\mu_\alpha \in \mathbb{M}_{\alpha,FE^2} \longrightarrow (\bar\mu_\alpha, \{\mu_{\alpha,i}^S\}) \in \bar{\mathbb{M}}_\alpha \times \left[\times_i \mathbb{M}_{\square,i,\alpha}^S\right]. \tag{18b}$$

Hence, there exist components $(\varphi^S, \mu_\alpha^S)$ and corresponding spaces $(\mathbb{P}_{\square,i}^S, \mathbb{M}_{\square,i,\alpha}^S)$ for each single RVE $\Omega_{\square,i}$ defined as

$$\mathbb{P}_\square^S := \{q \in \hat{\mathbb{P}}_\square : \ \bar\varphi_\square(q^S) = \bar{\boldsymbol{g}}_\square^\varphi(q^S) = 0\}, \tag{19a}$$

$$\mathbb{M}_{\square,\alpha}^S := \{q \in \hat{\mathbb{M}}_{\square,\alpha} : \ \bar\mu_{\square,\alpha}(q^S) = \bar{\boldsymbol{g}}_{\square,\alpha}^\mu(q^S) = 0\}, \tag{19b}$$

where $\hat{\mathbb{P}}_\square, \hat{\mathbb{M}}_{\square,\alpha}$ are suitable function spaces of same regularity as the underlying problem, that else define the boundary conditions needed to localize the RVE problem, cf. below.

We now restate the two-scale problem (9) as follows: Find $(\bar\varphi, \{\varphi_i^S\}, \bar\mu_\alpha, \{\mu_{\alpha,i}^S\}) \in \bar{\mathbb{P}} \times [\times_i \mathbb{P}_{\square,i}^S] \times \bar{\mathbb{M}}_\alpha \times [\times_i \mathbb{M}_{\square,i,\alpha}^S]$ that solve

$$\int_\Omega \left[\langle(\varphi^M[\delta\bar\varphi] + \delta\varphi^S)\rho\rangle_\square + \langle\boldsymbol{\nabla}(\varphi^M[\delta\bar\varphi] + \delta\varphi^S) \cdot \boldsymbol{d}\rangle_\square \right] d\Omega$$
$$= \int_{\Gamma_N^{(\varphi)}} \delta\bar\varphi \, \bar{d}^p \, d\Gamma \quad \forall(\delta\bar\varphi, \delta\varphi^S) \in \bar{\mathbb{P}}^0 \times [\times_i \mathbb{P}_{\square,i}^S], \tag{20a}$$

$$\int_\Omega \left[\phi \langle(\mu_\alpha^M[\delta\bar\mu_\alpha] + \delta\mu_\alpha^S)\partial_t c_\alpha\rangle_{\square,E} - \phi \langle\boldsymbol{\nabla}(\mu_\alpha^M[\delta\bar\mu_\alpha] + \delta\mu_\alpha^S) \cdot \boldsymbol{j}_\alpha\rangle_{\square,E} \right] d\Omega$$
$$= -\int_{\bar\Gamma_{N,\alpha}^{(\mu)}} \delta\bar\mu_\alpha \, \bar{j}_\alpha^p \, d\Gamma \quad \forall(\delta\bar\mu_\alpha, \delta\mu_\alpha^S) \in \bar{\mathbb{M}}_\alpha^0 \times [\times_i \mathbb{M}_{\square,i,\alpha}^S], \tag{20b}$$

$\alpha = 1, 2, \ldots N$, where we used, for convenience, the interpretation $\delta\varphi^S = \delta\varphi_i^S$ and $\delta\mu_\alpha^S = \delta\mu_{\alpha,i}^S$ inside $\Omega_{\square,i}$. Initial conditions are appropriately defined.

The homogenization gives that $\partial\Omega = \bar\Gamma_{N,\alpha}^{(\mu)} \cup \bar\Gamma_{D,\alpha}^{(\mu)}$, where $\bar\Gamma_{N,\alpha}$ denotes the homogenized boundary (as opposed to $\Gamma_{N,\alpha}^{(\mu)}$ only describing the electrolyte boundary). Furthermore, the flux boundary conditions are interpreted on the homogenized scale as $d^p \to \bar{d}^p$ and $j_\alpha^p \to \bar{j}_\alpha^p$. In the following, we shall assume $\bar{d}^p$ and $\bar{j}_\alpha^p$ to be the known data for the problem. Evaluation for known fine-scale fluxes would require surface homogenization.

3.2. Macro-scale problem

We obtain the homogenized macro-scale problem upon testing (20) with the purely macroscopic functions $\delta\bar\varphi \in \bar{\mathbb{P}}$ and $\delta\bar\mu_\alpha \in \bar{\mathbb{M}}_\alpha$. This gives

$$\int_\Omega \left[\langle(\varphi^M[\delta\bar\varphi])\rho\rangle_\square + \langle\boldsymbol{\nabla}(\varphi^M[\delta\bar\varphi]) \cdot \boldsymbol{d}\rangle_\square \right] d\Omega$$
$$= \int_{\Gamma_N^{(\varphi)}} \delta\bar\varphi \, \bar{d}^p \, d\Gamma \quad \forall\delta\bar\varphi \in \bar{\mathbb{P}}^0, \tag{21a}$$

$$\int_\Omega \left[\phi \langle(\mu_\alpha^M[\delta\bar\mu_\alpha])\partial_t c_\alpha\rangle_{\square,E} - \phi \langle\boldsymbol{\nabla}(\mu_\alpha^M[\delta\bar\mu_\alpha]) \cdot \boldsymbol{j}_\alpha\rangle_{\square,E} \right] d\Omega$$
$$= -\int_{\bar\Gamma_{N,\alpha}^{(\mu)}} \delta\bar\mu_\alpha \, \bar{j}_\alpha^p \, d\Gamma \quad \forall\delta\bar\mu_\alpha \in \bar{\mathbb{M}}_\alpha^0, \tag{21b}$$

which we can rewrite as

$$\int_\Omega \delta\bar\varphi \, \bar\rho + \boldsymbol{\nabla}\delta\bar\varphi \cdot \bar\rho^{(2)} + \boldsymbol{\nabla}\delta\bar\varphi \cdot \bar{\boldsymbol{d}} \, d\Omega = -\int_{\Gamma_N^{(\varphi)}} \delta\bar\varphi \, \bar{d}^p \, d\Gamma \quad \forall\delta\bar\varphi \in \bar{\mathbb{P}}^0, \tag{22a}$$

$$\int_\Omega \delta\bar\mu_\alpha \, \partial_t\bar{c}_\alpha + \boldsymbol{\nabla}\delta\bar\mu_\alpha \cdot \partial_t\bar{c}_\alpha^{(2)} - \boldsymbol{\nabla}\delta\bar\mu_\alpha \cdot \bar{\boldsymbol{j}}_\alpha \, d\Omega = -\int_{\bar\Gamma_{N,\alpha}^{(\mu)}} \delta\bar\mu_\alpha \, \bar{j}_\alpha^p \, d\Gamma \quad \forall\delta\bar\mu_\alpha \in \bar{\mathbb{M}}_\alpha^0, \tag{22b}$$

for $\alpha = 1, 2, \ldots, N$ together with the initial conditions

$$\bar{c}_\alpha(\boldsymbol{x}, 0) - \bar{c}_\alpha^{(2)}(\boldsymbol{x}, 0) \cdot \boldsymbol{\nabla} = \bar{c}_{\alpha,0} - \bar{c}_{\alpha,0}^{(2)} \cdot \boldsymbol{\nabla} \quad \text{in } \Omega_E, \tag{23a}$$

$$\bar{c}_\alpha^{(2)}(\boldsymbol{x}, 0) \cdot \boldsymbol{n} = \bar{c}_{\alpha,0}^{(2)} \cdot \boldsymbol{n} \quad \text{on } \partial\Omega_E, \tag{23b}$$

where $\bar{c}_{\alpha,0} := \phi \langle c_{\alpha,0}\rangle_{\square,E}$ and $\bar{c}_{\alpha,0}^{(2)} := \phi \langle c_{\alpha,0}[\boldsymbol{x} - \bar{\boldsymbol{x}}]\rangle_{\square,E}$.

Here, the variationally consistent macro-scale (homogenized) constitutive quantities are introduced as

$$\bar{\boldsymbol{d}} = \langle\boldsymbol{d}\rangle_\square = -\langle\boldsymbol{\epsilon} \cdot \boldsymbol{\nabla}\varphi\rangle_\square, \tag{24a}$$

$$\bar\rho = \langle\rho\rangle_\square = \phi \left\langle \sum_{\alpha=1}^N z_\alpha' c_\alpha \right\rangle_{\square,E}, \tag{24b}$$

$$\bar\rho^{(2)} = \langle\rho[\boldsymbol{x} - \bar{\boldsymbol{x}}]\rangle_\square, \tag{24c}$$

$$\bar{\boldsymbol{j}}_\alpha = \phi\langle\boldsymbol{j}_\alpha\rangle_{\square,E} = -\phi\langle\boldsymbol{M}_\alpha \cdot (\boldsymbol{\nabla}\mu_\alpha + z_\alpha'\boldsymbol{\nabla}\varphi)\rangle_{\square,E}, \tag{24d}$$

$$\bar{c}_\alpha = \phi\langle c_\alpha\rangle_{\square,E}, \tag{24e}$$

$$\bar{c}_\alpha^{(2)} = \phi \langle c_\alpha [\boldsymbol{x} - \bar{\boldsymbol{x}}] \rangle_{\square,\mathrm{E}}, \tag{24f}$$

$$\bar{\boldsymbol{\imath}} = \sum_\alpha z'_\alpha \bar{\boldsymbol{\jmath}}_\alpha, \tag{24g}$$

where (24c) and (24f) are non-standard higher order conservation quantities.

We are now in the position to identify the strong form of the balance equations as

$$\bar{\rho} - \bar{\rho}^{(2)} \cdot \boldsymbol{\nabla} - \bar{\boldsymbol{d}} \cdot \boldsymbol{\nabla} = 0 \quad \text{in } \Omega, \tag{25a}$$

$$\partial_t \bar{c}_\alpha - \partial_t \bar{c}_\alpha^{(2)} \cdot \boldsymbol{\nabla} + \bar{\boldsymbol{\jmath}}_\alpha \cdot \boldsymbol{\nabla} = 0 \quad \text{in } \Omega_\mathrm{E}. \tag{25b}$$

Motivated from (25), we introduce the effective fluxes

$$\bar{\boldsymbol{d}}_{\mathrm{eff}} = \bar{\boldsymbol{d}} + \bar{\rho}^{(2)}, \tag{26a}$$

$$\bar{\boldsymbol{\jmath}}_{\alpha,\mathrm{eff}} = \bar{\boldsymbol{\jmath}}_\alpha - \partial_t \bar{c}_\alpha^{(2)}, \tag{26b}$$

which are the effective fluxes that pertain to the original forms of the problem on the lower scale in (1). Therefore, the Neumann boundary conditions are (similarly as in Larsson et al. (2010)) defined as

$$\bar{\boldsymbol{d}}_{\mathrm{eff}} \cdot \boldsymbol{n} = \bar{d}^\mathrm{p}, \tag{27a}$$

$$\bar{\boldsymbol{\jmath}}_{\alpha,\mathrm{eff}} \cdot \boldsymbol{n} = \bar{\jmath}_\alpha^\mathrm{p}. \tag{27b}$$

Remark. With (24) and (1b), the effective macroscopic mass flux $\bar{\boldsymbol{\jmath}}_{\alpha,\mathrm{eff}}$ can be expressed as

$$\bar{\boldsymbol{\jmath}}_{\alpha,\mathrm{eff}} = \phi \left\langle \left([\boldsymbol{x} - \bar{\boldsymbol{x}}] \otimes \boldsymbol{\jmath}_\alpha \right) \cdot \boldsymbol{\nabla} \right\rangle_{\square,\mathrm{E}} = \frac{1}{|\Omega_\square|} \int_{\Gamma_{\square,\mathrm{E}}} \jmath_\alpha [\boldsymbol{x} - \bar{\boldsymbol{x}}] \, \mathrm{d}\Gamma. \tag{28}$$

Moreover, one can show that

$$\bar{\boldsymbol{d}}_{\mathrm{eff}} = \left\langle \left([\boldsymbol{x} - \bar{\boldsymbol{x}}] \otimes \boldsymbol{d} \right) \cdot \boldsymbol{\nabla} \right\rangle_\square = \frac{1}{|\Omega_\square|} \int_{\Gamma_\square} d[\boldsymbol{x} - \bar{\boldsymbol{x}}] \mathrm{d}\Gamma. \tag{29}$$

Hence, $\bar{\boldsymbol{\jmath}}_{\alpha,\mathrm{eff}}$ and $\bar{\boldsymbol{d}}_{\mathrm{eff}}$ pertain to the fluxes on the boundary of an RVE. $\square$

3.3. Micro-scale problem on a Representative Volume Element

In the previous Section, the macro-scale problem was defined, and it was established that the macro-scale fields in (22) depend on (φ, μ_α) inside the pertinent $\Omega_\square$. We shall now consider the local problem on a single RVE $\Omega_{\square,i}$ to determine the implicit relation $(\varphi_i^\mathrm{S}, \mu_{\alpha,i}^\mathrm{S})\{\bar{\varphi}, \bar{\mu}_\alpha\}$, where $\varphi|_{\Omega_{\square,i}} = \varphi^\mathrm{M}[\bar{\varphi}] + \varphi_i^\mathrm{S}$ and $\mu_\alpha|_{\Omega_{\square,i}} = \mu_\alpha^\mathrm{M}[\bar{\mu}_\alpha] + \mu_{\alpha,i}^\mathrm{S}$. To this end, we consider the problem in (20) for a single test function $\delta\varphi_i^\mathrm{S} \in \mathbb{P}_{\square,i}^\mathrm{S}$ and $\delta\mu_{\alpha,i}^\mathrm{S} \in \mathbb{M}_{\square,i,\alpha}^\mathrm{S}$. For brevity, we henceforth drop index i since we now restrict to one single RVE.

The decomposition in (11) presumes that the solution (φ, μ_α) can be uniquely decomposed into macroscopic parts $(\varphi^\mathrm{M}, \mu_\alpha^\mathrm{M})$ and fluctuations $(\varphi^\mathrm{S}, \mu_\alpha^\mathrm{S})$. This imposes constraints on $\mathbb{P}_\square^\mathrm{S}$ and $\mathbb{M}_{\square,\alpha}^\mathrm{S}$ in (16) and (17). In order to be explicit, we shall consider an expanded format of the problem. To this end, we introduce the richer spaces as follows:

$$\mathbb{P}_\square = \mathrm{H}^1(\Omega_\square), \quad \mathbb{M}_{\square,\alpha} = \mathrm{H}^1(\Omega_\square), \tag{30}$$

where $\mathrm{H}^1(\bullet)$ is the Sobolev space of functions with square integrable derivatives.

In order to ensure a uniquely solvable RVE-problem $(\varphi^\mathrm{S}, \mu_\alpha^\mathrm{S})$ with properly defined homogenization and scale bridging, we enforce

(i) fluctuation fields φ^S and μ_α^S to be periodic, i.e.

$$[\![\varphi^\mathrm{S}]\!]_\square(\boldsymbol{x}) = 0 \quad \forall \boldsymbol{x} \in \Gamma_\square^+, \quad [\![\mu_\alpha^\mathrm{S}]\!]_\square(\boldsymbol{x}) = 0 \quad \forall \boldsymbol{x} \in \Gamma_{\square,\mathrm{E}}^+, \tag{31}$$

where the difference operator is defined as $[\![\bullet]\!]_\square(\boldsymbol{x}) := \bullet(\boldsymbol{x}) - \bullet(\boldsymbol{x}^-(\boldsymbol{x}))$. Here, $\boldsymbol{x} \in \Gamma_\square^+$ is an image point whereas $\boldsymbol{x}^-(\boldsymbol{x}) \in \Gamma^- = \Gamma_\square \setminus \Gamma_\square^+$ is the corresponding mirror point. As previously mentioned in (12) and (14), the goal is to fulfill $\bar{g}_\square^\varphi(\varphi) = \bar{g}^\varphi$ and $\bar{g}_{\square,\alpha}^\mu(\mu_\alpha) = \bar{g}_\alpha^\mu$, which in turn will satisfy $\bar{g}_\square^\varphi(\varphi^\mathrm{S}) = \boldsymbol{0}$ and $\bar{g}_{\square,\alpha}^\mu(\mu_\alpha^\mathrm{S}) = \boldsymbol{0}$. With periodic φ^S and μ_α^S, the conditions

$\bar{g}_\square^\varphi(\varphi^\mathrm{S}) = \boldsymbol{0}$ and $\bar{g}_{\square,\alpha}^\mu(\mu_\alpha^\mathrm{S}) = \boldsymbol{0}$ are automatically satisfied due to the construction of the operators $\bar{g}_\square^\varphi$ and $\bar{g}_{\square,\alpha}^\mu$.

(ii) volume average constraints

$$\bar{\varphi}_\square(\varphi) = \bar{\varphi}, \quad \bar{\mu}_{\square,\alpha}(\mu_\alpha) = \bar{\mu}_\alpha. \tag{32}$$

We may express the variational (weak) statements of the micro-periodicity constraints in (31) as

$$\frac{1}{|\Omega_\square|} \int_{\Gamma_\square^+} \delta\lambda^{(\varphi)} [\![\varphi]\!]_\square \, \mathrm{d}\Gamma$$
$$= \left[\frac{1}{|\Omega_\square|} \int_{\Gamma_\square^+} \delta\lambda^{(\varphi)} [\![\boldsymbol{x}]\!]_\square \, \mathrm{d}\Gamma \right] \cdot \bar{\boldsymbol{g}}^\varphi \quad \forall \delta\lambda^{(\varphi)} \in \mathbb{T}_\square^{(\varphi)}, \tag{33a}$$

$$\frac{1}{|\Omega_\square|} \int_{\Gamma_{\square,\mathrm{E}}^+} \delta\lambda_\alpha^{(\mu)} [\![\mu_\alpha]\!]_\square \, \mathrm{d}\Gamma$$
$$= \left[\frac{1}{|\Omega_\square|} \int_{\Gamma_{\square,\mathrm{E}}^+} \delta\lambda_\alpha^{(\mu)} [\![\boldsymbol{x}]\!]_\square \, \mathrm{d}\Gamma \right] \cdot \bar{\boldsymbol{g}}_\alpha^\mu \quad \forall \delta\lambda_\alpha^{(\mu)} \in \mathbb{T}_\square^{(\mu)}, \tag{33b}$$

where it is used that $[\![\bar{\boldsymbol{x}}]\!]_\square = \boldsymbol{0}$. The Lagrange multipliers $\lambda^{(\varphi)}$ and $\lambda_\alpha^{(\mu)}$ can be identified as fields of virtual electric boundary fluxes and virtual boundary fluxes of charged particles on $\Gamma_\square^+$ and $\Gamma_{\square,\mathrm{E}}^+$. Here, we introduce the test spaces

$$\mathbb{T}_\square^{(\varphi)} = \mathrm{L}_2(\Gamma_\square^+), \quad \mathbb{T}_\square^{(\mu)} = \mathrm{L}_2(\Gamma_{\square,\mathrm{E}}^+), \tag{34}$$

where $\mathrm{L}_2(\bullet)$ is the space of square integrable functions. Hence, we conclude that it is only the data $\bar{\boldsymbol{g}}^\varphi$ and $\bar{\boldsymbol{g}}_\alpha^\mu$ that will have an effect on the periodicity conditions. For more information on weakly periodic boundary conditions, the reader is referred to Larsson et al. (2011). Similarly, the volume average constraints in (32) can be expressed as

$$\delta\hat{\lambda}^{(\varphi)} \langle\varphi\rangle_\square = \delta\hat{\lambda}^{(\varphi)} \bar{\varphi} \quad \forall \delta\hat{\lambda}^{(\varphi)} \in \mathbb{R}, \tag{35a}$$

$$\delta\hat{\lambda}_\alpha^{(\mu)} \langle\mu_\alpha\rangle_{\square,\mathrm{E}} = \delta\hat{\lambda}_\alpha^{(\mu)} (\bar{\mu}_\alpha + \bar{\boldsymbol{g}}_\alpha^\mu \cdot [\bar{\boldsymbol{x}}_\mathrm{E} - \bar{\boldsymbol{x}}]) \quad \forall \delta\hat{\lambda}_\alpha^{(\mu)} \in \mathbb{R}, \tag{35b}$$

where it is used that $\bar{g}_{\square,\alpha}^\mu(\mu_\alpha) = \bar{g}_\alpha^\mu$ since $\bar{g}_{\square,\alpha}^\mu(\mu_\alpha^\mathrm{S}) = \boldsymbol{0}$ from periodicity. With all RVE constraints in place, the aforementioned spaces in (19) can now be defined as

$$\mathbb{P}_\square^\mathrm{S} = \{q \in \mathbb{P}_\square : \int_{\Gamma_\square^+} \delta\lambda^{(\varphi)} [\![q]\!]_\square \, \mathrm{d}\Gamma = 0 \quad \forall \delta\lambda^{(\varphi)} \in \mathbb{T}_\square^{(\varphi)}, \ \langle q\rangle_\square = 0\}, \tag{36a}$$

$$\mathbb{M}_{\square,\alpha}^\mathrm{S} = \{q \in \mathbb{M}_{\square,\alpha} : \int_{\Gamma_{\square,\mathrm{E}}^+} \delta\lambda_\alpha^{(\mu)} [\![q]\!]_\square \, \mathrm{d}\Gamma = 0 \quad \forall \delta\lambda_\alpha^{(\mu)} \in \mathbb{T}_\square^{(\mu)}, \ \langle q\rangle_{\square,\mathrm{E}} = 0\}, \tag{36b}$$

such that

$$\bar{\varphi}_\square(q) = 0, \quad \bar{\boldsymbol{g}}_\square^{(\varphi)}(q) = \boldsymbol{0} \quad \forall q \in \mathbb{P}_\square^\mathrm{S}, \tag{37a}$$

$$\bar{\mu}_{\square,\alpha}(q) = 0, \quad \bar{\boldsymbol{g}}_{\square,\alpha}^{(\mu)}(q) = \boldsymbol{0} \quad \forall q \in \mathbb{M}_{\square,\alpha}^\mathrm{S}. \tag{37b}$$

The space-variational RVE-problem can then be stated as follows: For a given history $\bar{\varphi}(t)$, $\bar{\boldsymbol{g}}^\varphi(t)$, $\bar{\mu}_\alpha(t)$, $\bar{\boldsymbol{g}}_\alpha^\mu(t)$, $\alpha = 1, 2, \ldots, N$, find $\varphi(\bullet, t) \in \mathbb{P}_\square$, $\mu_\alpha(\bullet, t) \in \mathbb{M}_{\square,\alpha}$, $\lambda^{(\varphi)}(\bullet, t) \in \mathbb{T}_\square^{(\varphi)}$, $\lambda_\alpha^{(\mu)}(\bullet, t) \in \mathbb{T}_\square^{(\mu)}$, $\hat{\lambda}^{(\varphi)} \in \mathbb{R}$, $\hat{\lambda}_\alpha^{(\mu)} \in \mathbb{R}$ that solve

$$\sum_{\alpha=1}^N m_{\square,\alpha}^{(\varphi)}(\mu_\alpha, \delta\varphi) - a_\square^{(\varphi)}(\varphi, \delta\varphi) - \left\langle\left\langle \lambda^{(\varphi)} [\![\delta\varphi]\!]_\square \right\rangle\right\rangle_\square$$
$$- \hat{\lambda}^{(\varphi)} \langle\delta\varphi\rangle_\square = 0 \quad \forall \delta\varphi \in \mathbb{P}_\square, \tag{38a}$$

$$- \left\langle\left\langle \delta\lambda^{(\varphi)} [\![\varphi]\!]_\square \right\rangle\right\rangle_\square = - \left\langle\left\langle \delta\lambda^{(\varphi)} [\![\boldsymbol{x}]\!]_\square \right\rangle\right\rangle_\square \cdot \bar{\boldsymbol{g}}^\varphi \quad \forall \delta\lambda^{(\varphi)} \in \mathbb{T}_\square^{(\varphi)}, \tag{38b}$$

$$- \langle\varphi\rangle_\square \delta\hat{\lambda}^{(\varphi)} = -\bar{\varphi} \, \delta\hat{\lambda}^{(\varphi)} \quad \forall \delta\hat{\lambda}^{(\varphi)} \in \mathbb{R}, \tag{38c}$$

$$m_{\square,\alpha}^{(\mu)}(\partial_t\mu_\alpha, \delta\mu_\alpha) + a_{\square,\alpha}^{(\mu)}(\mu_\alpha, \delta\mu_\alpha) + a_{\square,\alpha}^{(\mu\varphi)}(\varphi, \delta\mu_\alpha)$$
$$+ \phi \left\langle\left\langle \lambda_\alpha^{(\mu)} [\![\delta\mu_\alpha]\!]_\square \right\rangle\right\rangle_{\square,\mathrm{E}} - \hat{\lambda}_\alpha^{(\mu)} \phi\langle\delta\mu_\alpha\rangle_{\square,\mathrm{E}} = 0 \quad \forall \delta\mu_\alpha \in \mathbb{M}_{\square,\alpha}, \tag{38d}$$

$$\phi \left\langle\left\langle \delta\lambda_\alpha^{(\mu)} [\![\mu_\alpha]\!]_\square \right\rangle\right\rangle_{\square,\mathrm{E}} = \phi \left\langle\left\langle \delta\lambda_\alpha^{(\mu)} [\![\boldsymbol{x}]\!]_\square \right\rangle\right\rangle_{\square,\mathrm{E}} \cdot \bar{\boldsymbol{g}}_\alpha^\mu \quad \forall \delta\lambda_\alpha^{(\mu)} \in \mathbb{T}_\square^{(\mu)}, \tag{38e}$$

$$- \phi\langle\mu_\alpha\rangle_{\square,\mathrm{E}} \delta\hat{\lambda}_\alpha^{(\mu)} = -\phi(\bar{\mu}_\alpha + \bar{\boldsymbol{g}}_\alpha^\mu \cdot [\bar{\boldsymbol{x}}_\mathrm{E} - \bar{\boldsymbol{x}}]) \delta\hat{\lambda}_\alpha^{(\mu)} \quad \forall \delta\hat{\lambda}_\alpha^{(\mu)} \in \mathbb{R}, \tag{38f}$$

with appropriately defined initial conditions. The pertinent RVE forms in (38) are given as

$$m_{\Box,\alpha}^{(\varphi)}(\mu_\alpha, \delta\varphi) := \frac{1}{|\Omega_\Box|} \int_{\Omega_\Box} z_\alpha' k_\alpha \mu_\alpha \, \delta\varphi \, d\Omega, \tag{39a}$$

$$a_\Box^{(\varphi)}(\varphi, \delta\varphi) := \frac{1}{|\Omega_\Box|} \int_{\Omega_\Box} \boldsymbol{\nabla}\delta\varphi \cdot \boldsymbol{\epsilon} \cdot \boldsymbol{\nabla}\varphi \, d\Omega, \tag{39b}$$

$$m_{\Box,\alpha}^{(\mu)}(\mu_\alpha, \delta\mu_\alpha) := \frac{1}{|\Omega_\Box|} \int_{\Omega_{\Box,E}} \mu_\alpha k_\alpha \, \delta\mu_\alpha \, d\Omega, \tag{39c}$$

$$a_{\Box,\alpha}^{(\mu)}(\mu_\alpha, \delta\mu_\alpha) := \frac{1}{|\Omega_\Box|} \int_{\Omega_{\Box,E}} \boldsymbol{\nabla}\delta\mu_\alpha \cdot \boldsymbol{M}_\alpha \cdot \boldsymbol{\nabla}\mu_\alpha \, d\Omega, \tag{39d}$$

$$a_{\Box,\alpha}^{(\mu,\varphi)}(\varphi, \delta\mu_\alpha) := \frac{1}{|\Omega_\Box|} \int_{\Omega_{\Box,E}} \boldsymbol{\nabla}\delta\mu_\alpha \cdot \boldsymbol{M}_\alpha \cdot z_\alpha' \boldsymbol{\nabla}\varphi \, d\Omega, \tag{39e}$$

with surface averaging operators defined as

$$\langle\!\langle \bullet \rangle\!\rangle_\Box := \frac{1}{|\Omega_\Box|} \int_{\Gamma_{\Box^+}} \bullet \, d\Gamma, \tag{40a}$$

$$\langle\!\langle \bullet \rangle\!\rangle_{\Box,E} := \frac{1}{|\Omega_{\Box,E}|} \int_{\Gamma_{\Box^+,E}} \bullet \, d\Gamma. \tag{40b}$$

Finally, with the full RVE problem at hand, we note the following properties pertaining to the problem:

(i) Setting $\delta\varphi = 1$ in (38a) results in $\hat{\lambda}^{(\varphi)} = \bar{\rho}$, and setting $\delta\varphi = [\boldsymbol{x} - \bar{\boldsymbol{x}}] \cdot \boldsymbol{e}_i$, $i = 1, 2, 3$, in (38a) results in $\langle\!\langle \langle \lambda^{(\varphi)} [\![\boldsymbol{x}]\!]_\Box \rangle \rangle\!\rangle_\Box = \bar{\boldsymbol{d}}_{\text{eff}}$. Similarly, setting $\delta\mu_\alpha = 1$ in (38d) results in $\hat{\lambda}_\alpha^{(\mu)} = \partial_t \bar{c}_\alpha$, and setting $\delta\mu_\alpha = [\boldsymbol{x} - \bar{\boldsymbol{x}}] \cdot \boldsymbol{e}_i$ in (38d) results in $\phi \langle\!\langle \langle \lambda_\alpha^{(\mu)} [\![\boldsymbol{x}]\!]_\Box \rangle \rangle\!\rangle_{\Box,E} = \bar{\boldsymbol{j}}_{\text{eff}} + \partial_t \bar{c}_\alpha [\bar{\boldsymbol{x}}_E - \bar{\boldsymbol{x}}]$. With the identified Lagrange multipliers, it is now possible to state the equivalent strong form as

$$\rho - \boldsymbol{d} \cdot \boldsymbol{\nabla} = \hat{\lambda}^{(\varphi)} \qquad \text{in } \Omega_\Box, \tag{41a}$$

$$\partial_t c_\alpha + \boldsymbol{j}_\alpha \cdot \boldsymbol{\nabla} = \hat{\lambda}_\alpha^{(\mu)} \qquad \text{in } \Omega_{\Box,E}, \tag{41b}$$

$$\boldsymbol{d} \cdot \boldsymbol{n} = \begin{cases} \lambda^{(\varphi)}(\bullet, t) & \text{on } \Gamma_\Box^+, \\ -\lambda^{(\varphi)}(\boldsymbol{x}^+(\bullet), t) & \text{on } \Gamma_\Box^-, \end{cases} \tag{41c}$$

$$\boldsymbol{j}_\alpha \cdot \boldsymbol{n} = \begin{cases} \lambda_\alpha^{(\mu)}(\bullet, t) & \text{on } \Gamma_{\Box,E}^+, \\ -\lambda_\alpha^{(\mu)}(\boldsymbol{x}^+(\bullet), t) & \text{on } \Gamma_{\Box,E}^-, \end{cases} \tag{41d}$$

where $\hat{\lambda}^{(\varphi)}$ corresponds to a uniform fictitious charge density in $\Omega_\Box$, $\hat{\lambda}_\alpha^{(\mu)}$ corresponds to a uniform ion source term in $\Omega_{\Box,E}$, $\lambda^{(\varphi)}$ and $\lambda_\alpha^{(\mu)}$ correspond to self-equilibrated boundary fluxes.

(ii) The solution (φ, μ_α) to (38) can be expressed as $(\varphi_0 + \bar{\varphi}, \mu_\alpha)$, where (φ_0, μ_α) is the solution to (38) with $\bar{\varphi} = 0$. Hence, all effective quantities in (24) are invariant to $\bar{\varphi}$.

(iii) Setting $\delta\varphi = \partial_t\varphi$, $\delta\mu_\alpha = \mu_\alpha$, $\delta\lambda^{(\varphi)} = \lambda^{(\varphi)}$, $\delta\lambda_\alpha^{(\mu)} = \lambda_\alpha^{(\mu)}$, and summing up all equations in (38) for all species, we are able to derive the relation

$$\sum_{\alpha=1}^N \phi \langle \mu_\alpha \partial_t c_\alpha \rangle_{\Box,E} - \sum_{\alpha=1}^N \phi \langle \boldsymbol{\nabla}\mu_\alpha \cdot \boldsymbol{j}_\alpha \rangle_{\Box,E} + \langle \partial_t \varphi \rho \rangle_\Box + \langle \boldsymbol{\nabla}\partial_t\varphi \cdot \boldsymbol{d} \rangle_\Box$$

$$= \sum_{\alpha=1}^N (\bar{\mu}_\alpha + \bar{\boldsymbol{g}}_\alpha^\mu \cdot [\bar{\boldsymbol{x}}_E - \bar{\boldsymbol{x}}]) \phi \hat{\lambda}_\alpha^{(\mu)} - \sum_{\alpha=1}^N \phi \langle\!\langle \langle [\![\boldsymbol{x}]\!]_\Box \lambda_\alpha^{(\mu)} \rangle \rangle\!\rangle_{\Box,E} \cdot \bar{\boldsymbol{g}}_\alpha^\mu$$

$$+ \partial_t\bar{\varphi} \, \hat{\lambda}^{(\varphi)} + \langle\!\langle \langle [\![\boldsymbol{x}]\!]_\Box \lambda^{(\varphi)} \rangle \rangle\!\rangle_\Box \cdot \partial_t\bar{\boldsymbol{g}}^\varphi. \tag{42}$$

Taking (24)–(26) into account, identifying $\hat{\lambda}^{(\varphi)} = \bar{\rho}$, $\phi\hat{\lambda}_\alpha^{(\mu)} = \partial_t\bar{c}_\alpha$ from (41), and using $\langle\!\langle \langle [\![\boldsymbol{x}]\!]_\Box \lambda^{(\varphi)} \rangle \rangle\!\rangle_\Box = \bar{\boldsymbol{d}}_{\text{eff}}$, $\phi \langle\!\langle \langle [\![\boldsymbol{x}]\!]_\Box \lambda_\alpha^{(\mu)} \rangle \rangle\!\rangle_{\Box,E}$ $= \bar{\boldsymbol{j}}_{\alpha,\text{eff}} + \partial_t\bar{c}_\alpha[\bar{\boldsymbol{x}}_E - \bar{\boldsymbol{x}}]$, we can derive the identity

$$\sum_{\alpha=1}^N \phi \langle \mu_\alpha \partial_t c_\alpha \rangle_{\Box,E} - \sum_{\alpha=1}^N \phi \langle \boldsymbol{\nabla}\mu_\alpha \cdot \boldsymbol{j}_\alpha \rangle_{\Box,E} + \langle \partial_t \varphi \rho \rangle_\Box + \langle \boldsymbol{\nabla}\partial_t\varphi \cdot \boldsymbol{d} \rangle_\Box$$

$$= \sum_{\alpha=1}^N \bar{\mu}_\alpha \partial_t\bar{c}_\alpha - \sum_{\alpha=1}^N \bar{\boldsymbol{j}}_{\alpha,\text{eff}} \cdot \bar{\boldsymbol{g}}_\alpha^\mu + \partial_t\bar{\varphi}\bar{\rho} + \bar{\boldsymbol{d}}_{\text{eff}} \cdot \partial_t\bar{\boldsymbol{g}}^\varphi. \tag{43}$$

This expression is precisely the macro-homogeneity condition. Therefore, it is a built-in property of the problem formulation.

3.4. Stationary part of the micro-scale problem

The RVE solution fields can be split into a stationary part and a transient part

$$\varphi(\boldsymbol{x}, t) = \varphi^{\text{stat}}(\boldsymbol{x}, t) + \varphi^{\text{trans}}(\boldsymbol{x}, t), \tag{44a}$$

$$\mu_\alpha(\boldsymbol{x}, t) = \mu_\alpha^{\text{stat}}(\boldsymbol{x}, t) + \mu_\alpha^{\text{trans}}(\boldsymbol{x}, t), \tag{44b}$$

where the notation stationary refers to the steady-state response corresponding to assumed sustained loading, i.e. solving the system under the assumption that $\partial_t\mu_\alpha = 0$, while transient refers to the response that contains relaxation processes when the loading is applied quickly as compared to the relaxation time.

For a given load $\bar{\varphi}(t)$, $\bar{\boldsymbol{g}}^\varphi(t)$, $\bar{\mu}_\alpha(t)$, $\bar{\boldsymbol{g}}_\alpha^\mu(t)$, for $\alpha = 1, 2, \ldots, N$ at every time instance t, find the stationary distributions $\varphi^{\text{stat}} \in \mathbb{P}_\Box$, $\mu_\alpha^{\text{stat}} \in \mathbb{M}_{\Box,\alpha}$, $\lambda^{(\varphi)} \in \mathbb{T}_\Box$, $\lambda_\alpha^{(\mu)} \in \mathbb{T}_\Box$, $\hat{\lambda}^{(\varphi)} \in \mathbb{R}$, $\hat{\lambda}_\alpha^{(\mu)} \in \mathbb{R}$ that solve

$$\sum_{\alpha=1}^N m_{\Box,\alpha}^{(\varphi)}(\mu_\alpha^{\text{stat}}, \delta\varphi) - a_\Box^{(\varphi)}(\varphi^{\text{stat}}, \delta\varphi) - \langle\!\langle \langle \lambda^{(\varphi)} [\![\delta\varphi]\!]_\Box \rangle \rangle\!\rangle_\Box$$

$$- \hat{\lambda}^{(\varphi)} \langle \delta\varphi \rangle_\Box = 0 \quad \forall\delta\varphi \in \mathbb{P}_\Box, \tag{45a}$$

$$- \langle\!\langle \langle \delta\lambda^{(\varphi)} [\![\varphi^{\text{stat}}]\!]_\Box \rangle \rangle\!\rangle_\Box = - \langle\!\langle \langle \delta\lambda^{(\varphi)} [\![\boldsymbol{x}]\!]_\Box \rangle \rangle\!\rangle_\Box \cdot \bar{\boldsymbol{g}}^\varphi \quad \forall\delta\lambda^{(\varphi)} \in \mathbb{T}_\Box^{(\varphi)}, \tag{45b}$$

$$- \langle \varphi^{\text{stat}} \rangle_\Box \delta\hat{\lambda}^{(\varphi)} = -\bar{\varphi} \, \delta\hat{\lambda}^{(\varphi)} \quad \forall\delta\hat{\lambda}^{(\varphi)} \in \mathbb{R}, \tag{45c}$$

$$a_{\Box,\alpha}^{(\mu)}(\mu_\alpha^{\text{stat}}, \delta\mu_\alpha) + a_{\Box,\alpha}^{(\mu\varphi)}(\varphi^{\text{stat}}, \delta\mu_\alpha)$$

$$+ \phi \langle\!\langle \langle \lambda_\alpha^{(\mu)} [\![\delta\mu_\alpha]\!]_\Box \rangle \rangle\!\rangle_{\Box,E} - \hat{\lambda}_\alpha^{(\mu)} \phi \langle \delta\mu_\alpha \rangle_{\Box,E} = 0 \quad \forall\delta\mu_\alpha \in \mathbb{M}_{\Box,\alpha}, \tag{45d}$$

$$\phi \langle\!\langle \langle \delta\lambda_\alpha^{(\mu)} [\![\mu_\alpha^{\text{stat}}]\!]_\Box \rangle \rangle\!\rangle_{\Box,E} = \phi \langle\!\langle \langle \delta\lambda_\alpha^{(\mu)} [\![\boldsymbol{x}]\!]_\Box \rangle \rangle\!\rangle_{\Box,E} \cdot \bar{\boldsymbol{g}}_\alpha^\mu \quad \forall\delta\lambda_\alpha^{(\mu)} \in \mathbb{T}_\Box^{(\mu)}, \tag{45e}$$

$$-\phi \langle \mu_\alpha^{\text{stat}} \rangle_{\Box,E} \delta\hat{\lambda}_\alpha^{(\mu)} = -\phi(\bar{\mu}_\alpha + \bar{\boldsymbol{g}}_\alpha^\mu \cdot [\bar{\boldsymbol{x}}_E - \bar{\boldsymbol{x}}]) \delta\hat{\lambda}_\alpha^{(\mu)} \quad \forall\delta\hat{\lambda}_\alpha^{(\mu)} \in \mathbb{R}. \tag{45f}$$

Remark. We do not distinguish the notation of the Lagrange multipliers upon solving the stationary and the transient problem, see Eq. (45) and (38) respectively.

Note that the stationary parts $\bullet^{\text{stat}}(\boldsymbol{x}, t)$ from (44) depend explicitly on the macroscopic loading histories
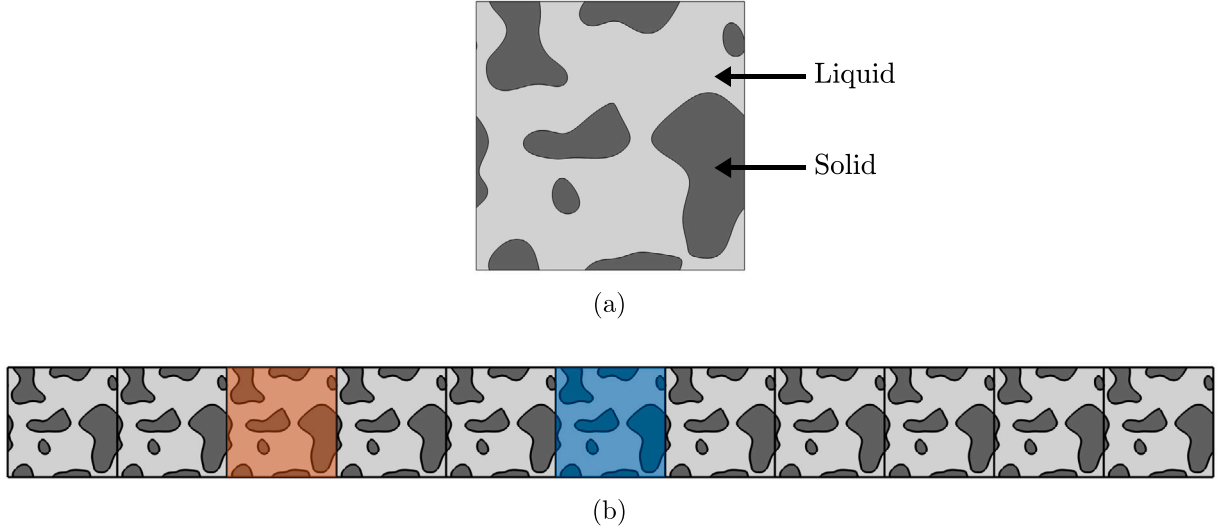
$$\varphi^{\text{stat}}(\boldsymbol{x}, t) = \varphi_{\bar{\varphi}}(\boldsymbol{x}) \bar{\varphi}(t) + \boldsymbol{\varphi}_{\bar{\boldsymbol{g}}^\varphi}(\boldsymbol{x}) \cdot \bar{\boldsymbol{g}}^\varphi(t)$$

$$+ \sum_{\alpha=1}^N \left(\varphi_{\bar{\mu}_\alpha}(\boldsymbol{x}) \bar{\mu}_\alpha(t) + \boldsymbol{\varphi}_{\bar{\boldsymbol{g}}_\alpha^\mu}(\boldsymbol{x}) \cdot \bar{\boldsymbol{g}}_\alpha^\mu(t) \right), \tag{46a}$$

$$\mu_\alpha^{\text{stat}}(\boldsymbol{x}, t) = \mu_{\alpha,\bar{\varphi}}(\boldsymbol{x}) \bar{\varphi}(t) + \boldsymbol{\mu}_{\alpha,\bar{\boldsymbol{g}}^\varphi}(\boldsymbol{x}) \cdot \bar{\boldsymbol{g}}^\varphi(t)$$

$$+ \sum_{\beta=1}^N \left(\mu_{\alpha,\bar{\mu}_\beta}(\boldsymbol{x}) \bar{\mu}_\beta(t) + \boldsymbol{\mu}_{\alpha,\bar{\boldsymbol{g}}_\beta^\mu}(\boldsymbol{x}) \cdot \bar{\boldsymbol{g}}_\beta^\mu(t) \right), \tag{46b}$$

where each sensitivity field $[\varphi_{\bar{\varphi}}, \boldsymbol{\varphi}_{\bar{\boldsymbol{g}}^\varphi}, \varphi_{\bar{\mu}_\alpha}, \boldsymbol{\varphi}_{\bar{\boldsymbol{g}}_\alpha^\mu}, \mu_{\alpha,\bar{\varphi}}, \boldsymbol{\mu}_{\alpha,\bar{\boldsymbol{g}}^\varphi}, \mu_{\alpha,\bar{\mu}_\beta}, \boldsymbol{\mu}_{\alpha,\bar{\boldsymbol{g}}_\beta^\mu}]$ is solved from a sensitivity problem as outlined in Appendix A. Inserting these expressions into the macro-scale constitutive quantities in (24) results in the following relations

$$\bar{\boldsymbol{d}}^{\text{stat}}(\boldsymbol{x}, t) = - \langle \boldsymbol{\epsilon} \cdot (\boldsymbol{\nabla} \otimes \boldsymbol{\varphi}_{\bar{\boldsymbol{g}}^\varphi}) \rangle_\Box \cdot \bar{\boldsymbol{g}}^\varphi(t) - \sum_{\alpha=1}^N \langle \boldsymbol{\epsilon} \cdot \boldsymbol{\nabla}\rho_{\bar{\mu}_\alpha} \rangle_\Box \bar{\mu}_\alpha(t)$$

$$- \sum_{\alpha=1}^N \langle \boldsymbol{\epsilon} \cdot (\boldsymbol{\nabla} \otimes \boldsymbol{\varphi}_{\bar{\boldsymbol{g}}_\alpha^\mu}) \rangle_\Box \cdot \bar{\boldsymbol{g}}_\alpha^\mu(t), \tag{47a}$$

$$\bar{\rho}^{\text{stat}}(\boldsymbol{x}, t) = \left(\phi \sum_{\alpha=1}^N \langle z_\alpha' k_\alpha \mu_{\alpha,\bar{\boldsymbol{g}}^\varphi} \rangle_{\Box,E} \right) \cdot \bar{\boldsymbol{g}}^\varphi(t)$$

$$+ \sum_{\beta=1}^N \left(\phi \sum_{\alpha=1}^N \langle z_\alpha' k_\alpha \mu_{\alpha,\bar{\mu}_\beta} \rangle_{\Box,E} \right) \bar{\mu}_\beta(t)$$

$$+ \sum_{\beta=1}^N \left(\phi \sum_{\alpha=1}^N \langle z_\alpha' k_\alpha \boldsymbol{\mu}_{\alpha,\bar{\boldsymbol{g}}_\beta^\mu} \rangle_{\Box,E} \right) \cdot \bar{\boldsymbol{g}}_\beta^\mu(t), \tag{47b}$$

(a)

(b)

Fig. 3. RVE in (a) represents the microstructure of the SBE. Liquid electrolyte domain and solid polymer domain are indicated by the arrows. RVE size is 500×500 nm^2, where $x \in [-250, 250]$ nm and $y \in [-250, 250]$ nm, i.e. the RVE is centered. DNS geometry in (b); subdomains DNS3 (left) and DNS6 (middle) are marked in orange and blue respectively. DNS domain size is 5.5×0.5 μm^2, where $x \in [-2.75, 2.75]$ μm and $y \in [-250, 250]$ nm.

Table 1

Summary of steps for 2D RVE study.

(i)	Consider a 2D DNS geometry consisting of 2D RVEs that pertain to a repetitive structure, see Fig. 3
(ii)	Apply practically realizable macro-scale boundary conditions for DNS problem
(iii)	Solve DNS problem (8)
(iv)	Use volume averaging to measure and extract macro-scale fields ((12),(14)) and fluxes (24) from various DNS subdomains that are of the same size as the RVE domain
(v)	Prescribe extracted macro data for the RVE problem (38) based on prolongation rule (11) and predict the resulting fluxes
(vi)	Discuss numerical simulation results of the RVE problem versus the extracted data from DNS

$$\bar{\rho}^{(2),\text{stat}}(\boldsymbol{x},t) = \left(\phi \sum_{\alpha=1}^{N} \langle z'_\alpha k_\alpha \boldsymbol{\mu}_{\alpha,\bar{g}^\varphi} \otimes [\boldsymbol{x} - \bar{\boldsymbol{x}}] \rangle_{\square,\mathrm{E}} \right) \cdot \bar{\boldsymbol{g}}^\varphi(t)$$
$$+ \sum_{\beta=1}^{N} \left(\phi \sum_{\alpha=1}^{N} \langle z'_\alpha k_\alpha \boldsymbol{\mu}_{\alpha,\bar{\mu}_\beta} [\boldsymbol{x} - \bar{\boldsymbol{x}}] \rangle_{\square,\mathrm{E}} \right) \bar{\mu}_\beta(t)$$
$$+ \sum_{\beta=1}^{N} \left(\phi \sum_{\alpha=1}^{N} \langle z'_\alpha k_\alpha \boldsymbol{\mu}_{\alpha,\bar{g}^\mu_\beta} \otimes [\boldsymbol{x} - \bar{\boldsymbol{x}}] \rangle_{\square,\mathrm{E}} \right) \cdot \bar{\boldsymbol{g}}^\mu_\beta(t), \quad (47c)$$

$$\bar{\boldsymbol{j}}_\alpha^{\text{stat}}(\boldsymbol{x},t) = -\phi \langle \boldsymbol{M}_\alpha \cdot (\boldsymbol{\nabla} \otimes \boldsymbol{\mu}_{\alpha,\bar{g}^\varphi} + z'_\alpha \boldsymbol{\nabla} \otimes \boldsymbol{\varphi}_{\bar{g}^\varphi}) \rangle_{\square,\mathrm{E}} \cdot \bar{\boldsymbol{g}}^\varphi(t)$$
$$- \sum_{\beta=1}^{N} \phi \langle \boldsymbol{M}_\alpha \cdot (\boldsymbol{\nabla} \mu_{\alpha,\bar{\mu}_\beta} + z'_\alpha \boldsymbol{\nabla} \varphi_{\bar{\mu}_\beta}) \rangle_{\square,\mathrm{E}} \bar{\mu}_\beta(t)$$
$$- \sum_{\beta=1}^{N} \phi \langle \boldsymbol{M}_\alpha \cdot (\boldsymbol{\nabla} \otimes \boldsymbol{\mu}_{\alpha,\bar{g}^\mu_\beta} + z'_\alpha \boldsymbol{\nabla} \otimes \boldsymbol{\varphi}_{\bar{g}^\mu_\beta}) \rangle_{\square,\mathrm{E}} \cdot \bar{\boldsymbol{g}}^\mu_\beta(t), \quad (47d)$$

$$\bar{c}_\alpha^{\text{stat}}(\boldsymbol{x},t) = \left(\phi \langle k_\alpha \mu_{\alpha,\bar{g}^\varphi} \rangle_{\square,\mathrm{E}} \right) \cdot \bar{\boldsymbol{g}}^\varphi(t) + \sum_{\beta=1}^{N} \left(\phi \langle k_\alpha \mu_{\alpha,\bar{\mu}_\beta} \rangle_{\square,\mathrm{E}} \right) \bar{\mu}_\beta(t)$$
$$+ \sum_{\beta=1}^{N} \left(\phi \langle k_\alpha \boldsymbol{\mu}_{\alpha,\bar{g}^\mu_\beta} \rangle_{\square,\mathrm{E}} \right) \cdot \bar{\boldsymbol{g}}^\mu_\beta(t) + \left(\phi \langle c_{\alpha,0} \rangle_{\square,\mathrm{E}} \right), \quad (47e)$$

$$\bar{c}_\alpha^{(2),\text{stat}}(\boldsymbol{x},t) = \left(\phi \langle k_\alpha \boldsymbol{\mu}_{\alpha,\bar{g}^\varphi} \otimes [\boldsymbol{x} - \bar{\boldsymbol{x}}] \rangle_{\square,\mathrm{E}} \right) \cdot \bar{\boldsymbol{g}}^\varphi(t)$$
$$+ \sum_{\beta=1}^{N} \left(\phi \langle k_\alpha \mu_{\alpha,\bar{\mu}_\beta} [\boldsymbol{x} - \bar{\boldsymbol{x}}] \rangle_{\square,\mathrm{E}} \right) \bar{\mu}_\beta(t)$$
$$+ \sum_{\beta=1}^{N} \left(\phi \langle k_\alpha \boldsymbol{\mu}_{\alpha,\bar{g}^\mu_\beta} \otimes [\boldsymbol{x} - \bar{\boldsymbol{x}}] \rangle_{\square,\mathrm{E}} \right) \cdot \bar{\boldsymbol{g}}^\mu_\beta(t)$$
$$+ \left(\phi \langle c_{\alpha,0} [\boldsymbol{x} - \bar{\boldsymbol{x}}] \rangle_{\square,\mathrm{E}} \right), \quad (47f)$$

where we explicitly use the invariance following from solving the sensitivity problem with $\bar{\varphi} = 1$, i.e. $\varphi_{\bar{\varphi}} = 1 \rightarrow \boldsymbol{\nabla} \varphi_{\bar{\varphi}} = \boldsymbol{0}$ and $\mu_{\alpha,\bar{\varphi}} = 0$, cf. Appendix A.

4. Study of a single RVE and validation of upscaling

All simulations in the following numerical studies are performed using COMSOL Multiphysics. The first goal is to provide a numerical example via a 2D RVE study. Although a 2D RVE is insufficient to accurately model ion transport in SBEs (due to the lack of RVE bi-continuity), it allows for an inexpensive numerical validation study. A convenient way to study the time-dependent response of an RVE is by subjecting it to a consistent combination of loading histories $[\bar{\varphi}, \bar{\boldsymbol{g}}^\varphi, \bar{\mu}_\alpha, \bar{\boldsymbol{g}}^\mu_\alpha]$, see (38). In order to generate such a loading history, with relevant combination of the macroscopic fields and gradients, we will create a small 2D single scale problem in the upcoming section from which we can extract the loading histories of interest. The 2D single scale problem, henceforth denoted the 2D DNS, is solved in Section 4.1 with physically admissible macro-scale boundary conditions, i.e. in this case mimicking potentiostatic loading by prescribing the electric potential φ on the boundaries. The 2D DNS will also be used to evaluate the accuracy of the RVE upscaling in a validation step. Finally, in Section 4.2, the 2D RVE problem is investigated under the influence of the consistent combination of loading histories. Although the theory considers an arbitrary number of mobile species α, the current analysis will be restricted to only two mobile species, namely Li$^+$ and X$^-$.

The steps for performing the 2D RVE study are summarized in Table 1.

4.1. DNS of 2D single-scale problem

The computational domain of the 2D DNS is constructed such that it consists of 11 periodic 2D RVEs that are attached together in the x-direction. The RVE is a square domain with the side length 500 nm and is subdivided into a liquid domain and a solid domain, see Fig. 3. This RVE size is motivated by the fact that pore diameters in SBEs are
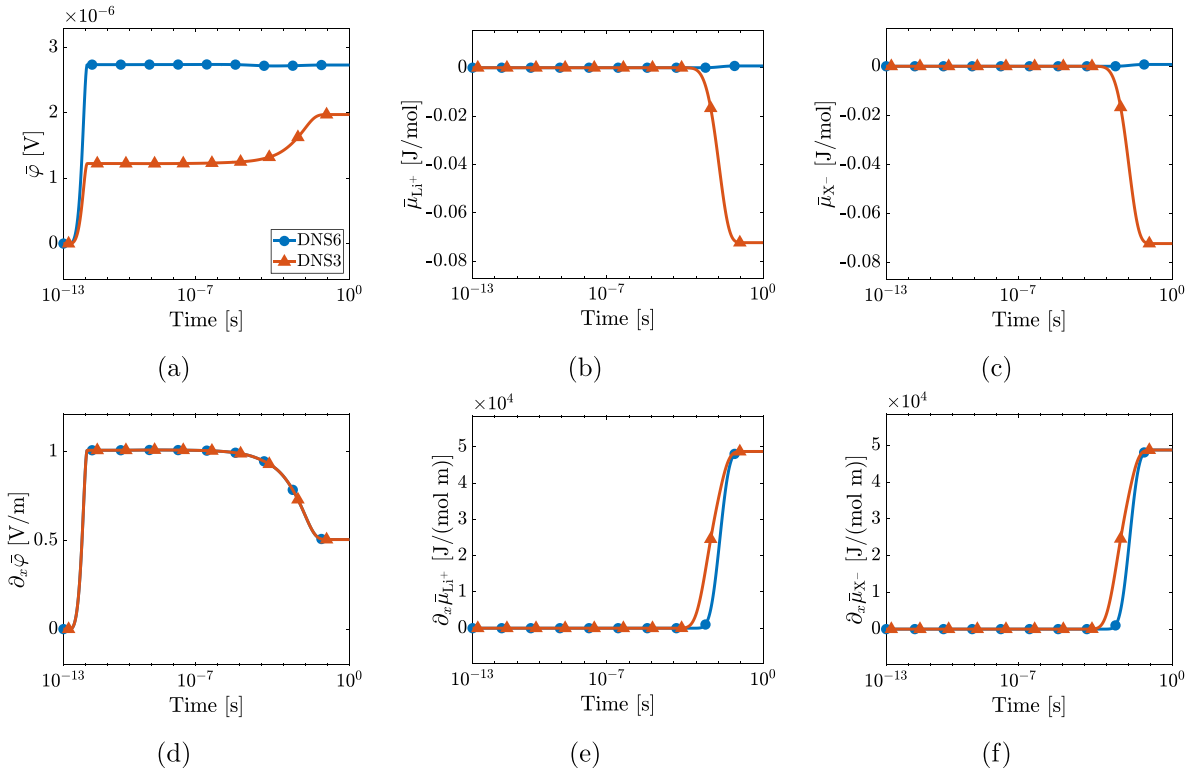
Fig. 4. Loading histories measured from DNS in subdomains DNS6 and DNS3.

Table 2
DNS boundary conditions.

Field	Left boundary	Right boundary	Top and bottom boundaries
φ	$\varphi^{\mathrm{p}} = 0$	Positive ramp $\varphi^{\mathrm{p}}(t)$	Periodicity in φ
μ_{Li^+}	$\mu_{\mathrm{Li}^+}^{\mathrm{p}} = 0$	$\mu_{\mathrm{Li}^+}^{\mathrm{p}} = 0$	Periodicity in μ_{Li^+}
μ_{X^-}	Zero flux condition	Zero flux condition	Periodicity in μ_{X^-}

found to be between 50-−200 nm (Ihrner et al., 2017; Schneider et al., 2019).

In the next step, the goal is to identify a consistent combination of loading histories for the RVE problem by subjecting the 2D DNS to a physically realistic loading case. This can be achieved by enforcing suitable boundary conditions, e.g. mimicking potentiostatic (prescribing electric potential) or galvanostatic (prescribing current density) loading. Here, we mimic the potentiostatic loading case. The right boundary is prescribed to an almost instantaneous ramp of electric potential, while the left boundary is fixed to zero electric potential. This ensures that an electric field is established in the 2D DNS domain, which causes the mobile species Li$^+$ and X$^-$ to move in opposite directions. Furthermore, the chemical potential of Li$^+$ is fixed to zero on both the left and right boundaries in order to allow for a non-zero stationary ionic flux through the boundaries. Hence, the Dirichlet boundary conditions on μ_{Li^+} act as an infinite sink and source. Meanwhile, the chemical potential of X$^-$ only have zero flux boundaries. Lastly, periodic boundary conditions are enforced on all fields on both the top and bottom boundaries. The boundary conditions are summarized in Table 2 and the material parameters are chosen according to Appendix B. The 2D DNS is spatially discretized using 118 200 quadratic triangular elements, resulting in a total of 538 295 degrees of freedom. The time stepping is performed with a BDF2 scheme using 500 time steps with exponential spacing.

After solving the 2D DNS, a consistent combination of 6 loading histories is identified, see Fig. 4. The goal is to apply this loading data on the RVE. All 6 loading histories are measured from the subdomains

DNS6 and DNS3, illustrated in Fig. 3, according to the homogenization operators defined in (12) and (14). Note here that the loading histories are different depending on if they are measured from DNS6 or DNS3. This can be explained by the fact that subdomain DNS6 is in the center, i.e. symmetric boundary conditions result in symmetric chemical potential distributions. Hence, the chemical potentials are close to zero in the center of subdomain DNS6, but non-zero in subdomain DNS3.

As an example of consistent data, the macroproblem will result in effective combinations of $\bar{\mu}_{\mathrm{Li}^+}$ and $\bar{\mu}_{\mathrm{X}^-}$ that approximately satisfy electro-neutrality, i.e. such that $\bar{\rho} \approx 0$. A net charge within the RVE would result in a large reaction term in the effective Gauss law (25a). This can clearly be identified in Figs. 4(b) and 4(c), where we note that $\bar{\mu}_{\mathrm{Li}^+} \approx \bar{\mu}_{\mathrm{X}^-}$ in each RVE.

4.2. RVE study in 2D

With the consistent combination of loading data at hand, the 2D RVE problem (38) is solved using periodic boundary conditions on fluctuation fields. The 2D RVE problem is spatially discretized using 21 434 quadratic triangular elements, resulting in a total of 98 710 degrees of freedom. Once again, the time stepping is performed with a BDF2 scheme using 500 time steps with exponential spacing. Effective fluxes are presented in Fig. 5. The results for the fully transient RVE-problem in (38) and the micro-stationary approximation in (45) are compared to the fluxes extracted from the DNS.

It can be seen from the validation results in Fig. 5 that the RVE upscaling error, when applying loading data extracted from DNS6, is negligible. This confirms that the RVE upscaling does indeed approximate the single-scale problem well around the center subdomain DNS6.

However, when the identified loading histories from DNS3 are prescribed on the RVE problem, a non-negligible error is obtained on the ionic flux terms in Figs. 5(e) and 5(f). This suggests that the RVE upscaling has a range of higher validity around the center subdomain. A reason that explains the ionic flux errors is that the two-scale model
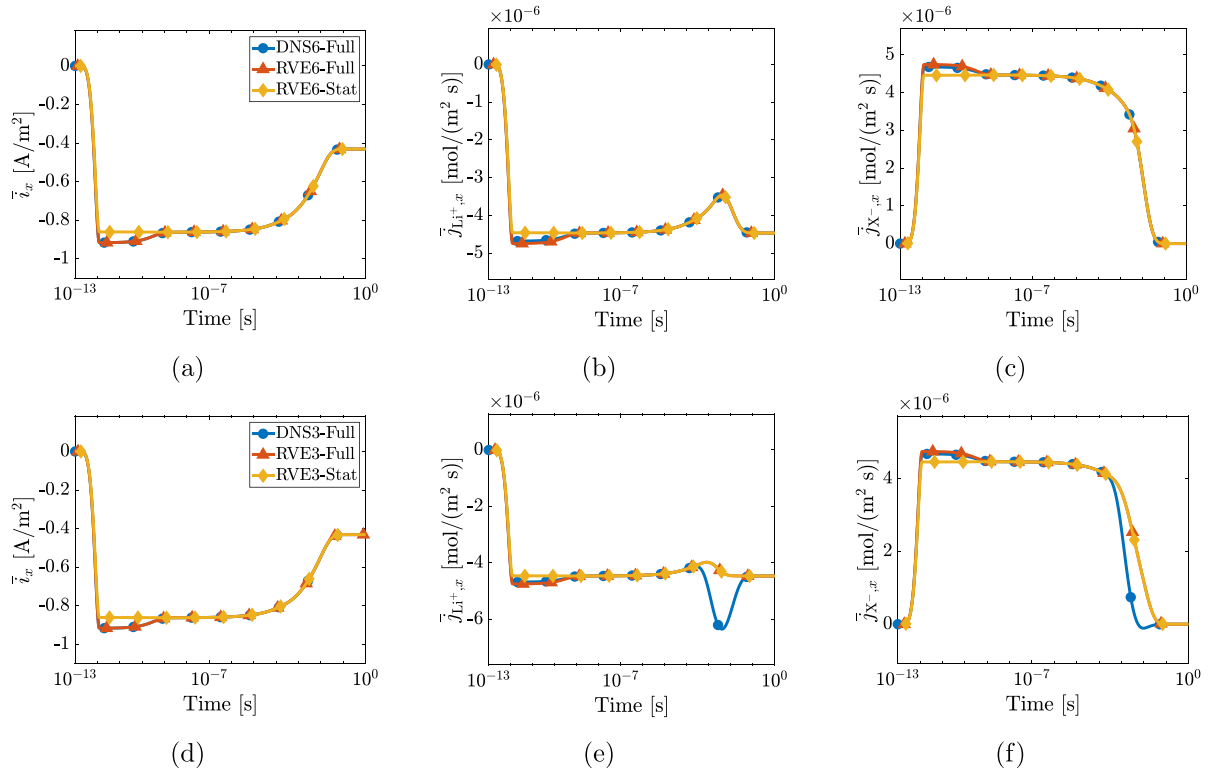
Fig. 5. Upscaled effective fluxes w.r.t. time. DNS6/3 refers to fluxes extracted from subdomain DNS6/3 in DNS, while RVE6/3 represents RVE-simulations based on loading data extracted from subdomain DNS6/3. Full and Stat refer to fully transient and micro-stationary, respectively.

cannot properly approximate the single-scale problem over the full domain when there is a lack of length scale separation, i.e. the single-scale domain is not sufficiently much larger than the RVE. Another possible explanation to this is that the RVE upscaling is sensitive to the loading data that pertain to $\bar{\mu}_{Li^+}(t)$ and $\bar{\mu}_{X^-}(t)$ as seen in Figs. 4(b) and 4(c). Although there are discrepancies in the ionic fluxes in Figs. 5(e) and 5(f), their respective error cancels out each other when the macroscopic current density $\bar{i}$ is computed as a post-processed quantity.

At the beginning of the flux curves in Fig. 5, we note that the difference between the stationary and the fully transient solution is small. Therefore, we conclude that the transient effects in the RVE are small for the considered length scales, and note that they only exist at the beginning of the simulation before $t = 10^{-9}$ s. This suggests that we can approximate the full RVE solution with its stationary counterpart for the considered application, especially if we assume that all transport processes before $t = 10^{-9}$ s are out of interest. This allows us to pre-compute upscaled coefficients, once and for all, which can be exploited to efficiently solve a macro-scale problem instead of solving the corresponding computationally expensive FE^2 problem. The proposed solution scheme is investigated in detail in Section 5. For simplicity, we will restrict the upcoming macro-scale validation study in Section 5 to the subdomain DNS6 in order to circumvent the non-negligible errors that arise in other subdomains of the DNS.

5. Computational results from upscaled problem

By assuming that the transient effects in the RVE are negligible, then the two-scale model can be solved in an efficient fashion by pre-computing constitutive quantities based on the stationary RVE problem. A numerical example is provided in Section 5.1. The upscaled problem is investigated by following the steps outlined in Table 3.

5.1. Validation of upscaled macro-scale problem formulation

The macro-scale problem consists of a seemingly homogeneous computational domain, see Fig. 6(a). Since the distinct phases of the microstructure are no longer resolved, an effective material which represents the homogenization of the liquid and solid phases is obtained. The macro-scale problem is solved with pre-computed coefficients according to the same boundary conditions as stated in Table 2. The mesh consists 12 130 quadratic triangular elements, resulting in a total of 74 565 degrees of freedom. The time stepping is performed with a BDF2 scheme using 500 time steps with exponential spacing. See Fig. 7 for the results.

Based on the results in Fig. 7, it is clear that the electrochemical system possesses multiple time scales. As mentioned earlier in Section 4.1, the choice of boundary conditions in Table 2 causes the electric potential to be fully ramped by $t = 10^{-12}$ s which gives rise to an electric field. The electric field causes an ionic migration of both species in each direction, see Fig. 9. During this time frame, the ionic migration is stationary and the chemical potentials have not yet started redistributing. The electrochemical system stays relatively constant until ca. $t = 10^{-4}$ s before the chemical potential distributions start changing substantially.

In the stationary limit, due to the boundary conditions on μ_{Li^+} and j_{X^-} respectively, we will obtain a net flux of Li-ions, while $j_{X^-} \to 0$. This means that μ_{X^-} will align with φ since $\boldsymbol{j}_{X^-} = \boldsymbol{M}_{X^-}(\boldsymbol{\nabla}\mu_{X^-} + z'_{X^-}\boldsymbol{\nabla}\varphi)$. Gauss law will in turn cause μ_{Li^+} to adapt according to μ_{X^-} in order to achieve electro-neutrality in the interior of the domain. The homogeneous Dirichlet boundary conditions on μ_{Li^+}, that act as an infinite sink and source, result in an abrupt change of μ_{Li^+} at the boundary that causes a deviation from electro-neutrality locally. This induces steep gradients of the electric potential φ close to the boundaries in order to balance out the net volume charge density in Gauss law. Here, we note that the steep gradients in electric potential φ at the boundaries results in a reduction in magnitude of the electric field in the domain.
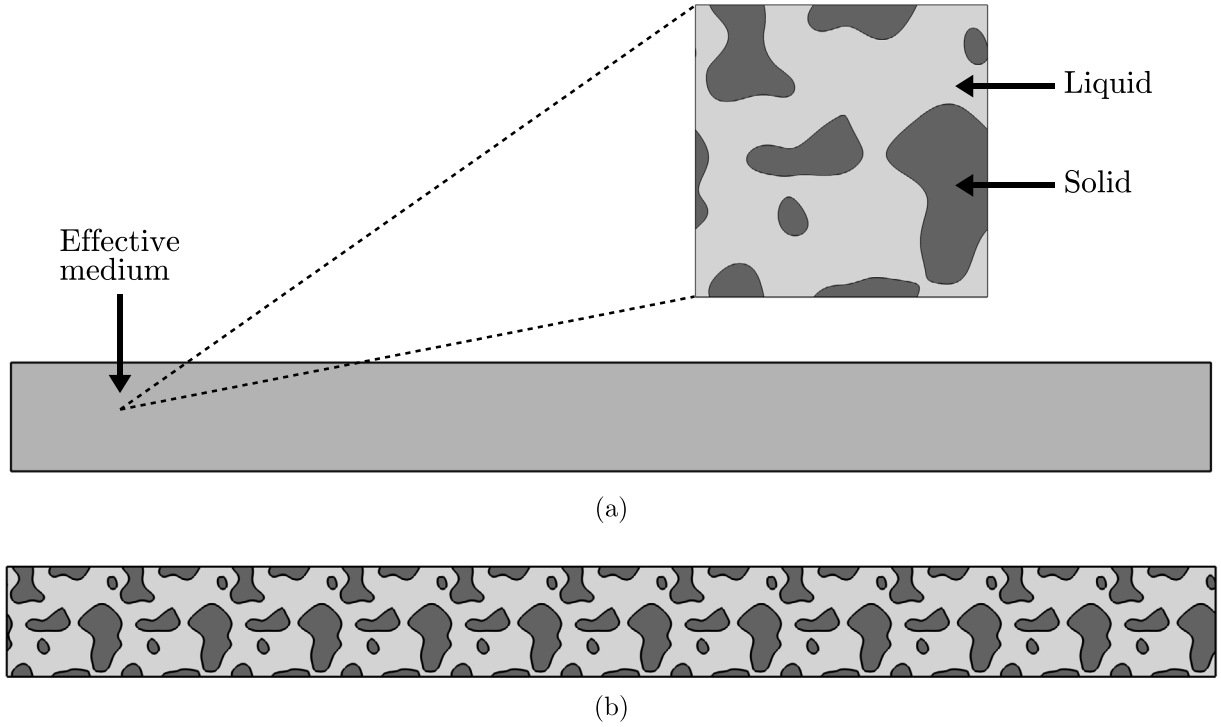
Fig. 6. (a) Assumed proper scale separation in two-scale model, and (b) small DNS with a length scale ratio of 11 between domain and RVE size, i.e. the RVE features are large compared to the DNS domain. RVE size is 500×500 nm^2 and macro-scale/DNS domain size is 5.5×0.5 μm^2.

Table 3

Outline of upscaled problem based on stationary 2D RVE.

(i)	Pre-compute effective coefficients for effective fluxes and storage terms according to (47), which is made possible by solving the linear stationary 2D RVE problem (45) instead of the linear transient 2D RVE problem (38)
(ii)	Consider a smooth macro-scale geometry in 2D that is comparable to the 2D DNS geometry
(iii)	Apply the same type of boundary conditions that were used in the DNS problem
(iv)	Solve macro-scale problem (21)
(v)	Discuss and validate the results against the DNS solution

Note that the volume charge density and the concentration distributions are, unlike the primary fields, not fully anti-symmetric. The reason is because of the so-called "scale mixing" effect. The higher order macro-scale storage terms in (24c) and (24g) depend on the difference $[x-\bar{x}]$, which in turn contains both the spatial RVE coordinate x and the spatial macro-scale coordinate $\bar{x}$. This implies that the RVE size and the macro-scale domain size will have a significant impact on the upscaled constitutive fluxes via higher order storage terms when the length scale difference between them is insufficient. Hence, the current length scale ratio between the macro-scale domain and RVE of 11 is insufficient. More on the scale mixing effect in Section 5.2.

In the next step, the aim is to validate the 2D macro-scale solution. Due to the trivial macro-scale geometry, there is no electric potential nor chemical potential variation in the vertical direction. Therefore, the 2D macro-scale problem can be reduced to a 1D problem. In order to validate the 2D macro-scale solution at stationarity, we use the analytical stationary 1D governing equations as follows

$$z' \left(c_{\text{Li}} - c_{\text{X}} \right) + \varepsilon \varphi'' = 0, \tag{48a}$$

$$-M_{\text{Li}} \left(\mu''_{\text{Li}} + z' \varphi'' \right) = 0, \tag{48b}$$

$$-M_{\text{X}} \left(\mu''_{\text{X}} - z' \varphi'' \right) = 0, \tag{48c}$$

where the computational domain is $x \in [-L, L]$ and $z' = |z'_{\text{Li}^+}| = |z'_{\text{X}^-}|$. The analytical solution, when prescribing analogous boundary conditions as stated in Table 2, becomes

$$\varphi(x) = \frac{\Delta\varphi}{2} \left[(1-\beta) \frac{e^{\alpha \frac{x}{L}} - e^{-\alpha \frac{x}{L}}}{e^{\alpha} - e^{-\alpha}} + \beta \frac{x}{L} + 1 \right], \tag{49a}$$

$$\mu_{\text{X}^-}(x) = z' \varphi(x), \tag{49b}$$

$$\mu_{\text{Li}^+}(x) = z' \frac{\Delta\varphi}{2} \left(\frac{x}{L} \right) - z' \varphi(x), \tag{49c}$$

$$\alpha = \sqrt{\frac{c'_{\text{Li}} + c'_{\text{X}}}{\varepsilon}} \, z' L, \tag{49d}$$

$$\beta = \frac{c'_{\text{Li}}}{c'_{\text{Li}} + c'_{\text{X}}}, \tag{49e}$$

where $\Delta\varphi$ corresponds to the final value of the prescribed ramp of electric potential $\varphi^{\text{p}}(t)$ on the right boundary, and $c'_\alpha = k_\alpha = \frac{c_{\alpha,0}}{RT}$ for $\alpha = \text{Li}, \text{X}$. After inserting the same pre-computed effective parameters into the 1D solution as in the smooth 2D macro-scale problem, we obtain matching stationary potential fields as seen in Fig. 8. Note here that we are able to analytically identify the same magnitude reduction of the electric field, during the charge accumulation at the boundaries as seen in the simulation, if we study the spatial derivative of the analytic electric potential

$$\partial_x \varphi(x = 0) = \frac{\Delta\varphi}{2L} \left[(1-\beta) \frac{2\alpha}{e^{\alpha} - e^{-\alpha}} + \beta \right], \tag{50}$$

setting $\beta = \frac{1}{2}$ and letting $\alpha \to \infty$ results in[2]

$$\partial_x \varphi(x = 0) \to \frac{\Delta\varphi}{4L}, \tag{51a}$$

---

[2] For the used material data, $\alpha = \sqrt{(c'_{\text{Li}} + c'_{\text{X}})/\varepsilon} \, z' L$, which in practice equals the infinite limit in the expressions (50) and (49a).
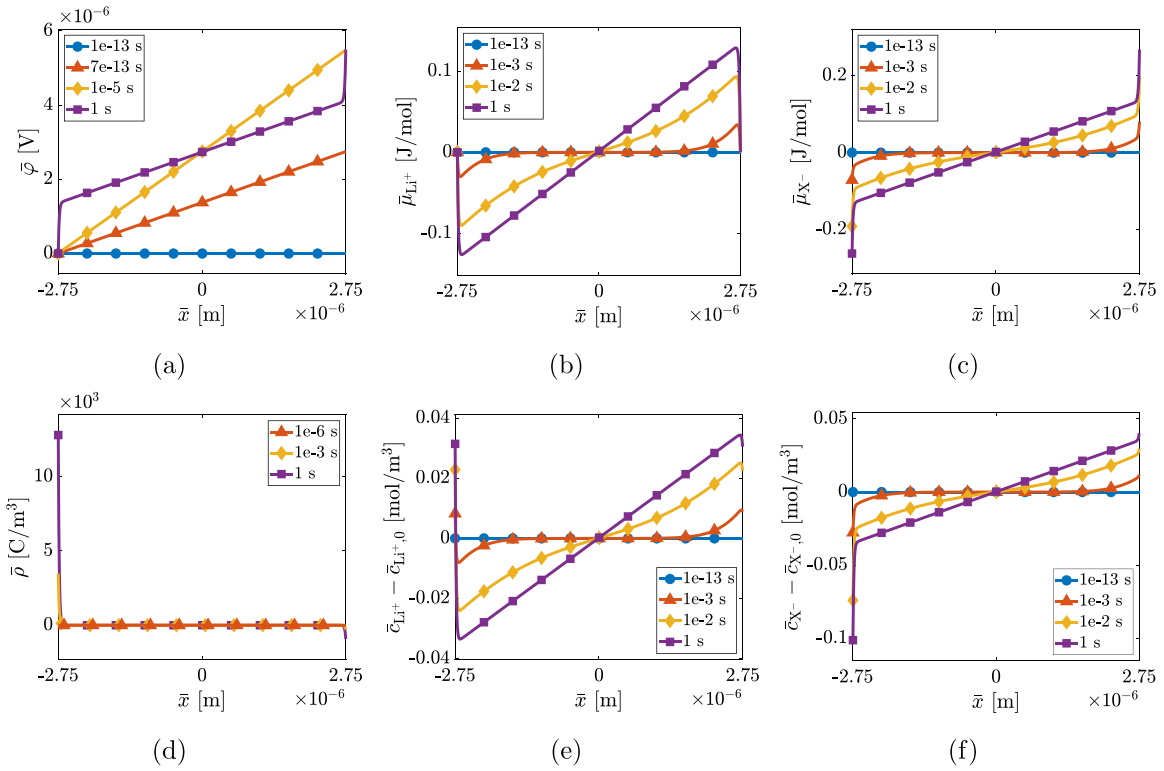
Fig. 7. Evaluation of scalar fields along the horizontal middle line in the macro-scale domain; (a) electric potential, (b) chemical potential of Li-ions, (c) chemical potential of X-ions, (d) volume charge density, (e) concentration of Li-ions and (f) concentration of X-ions.
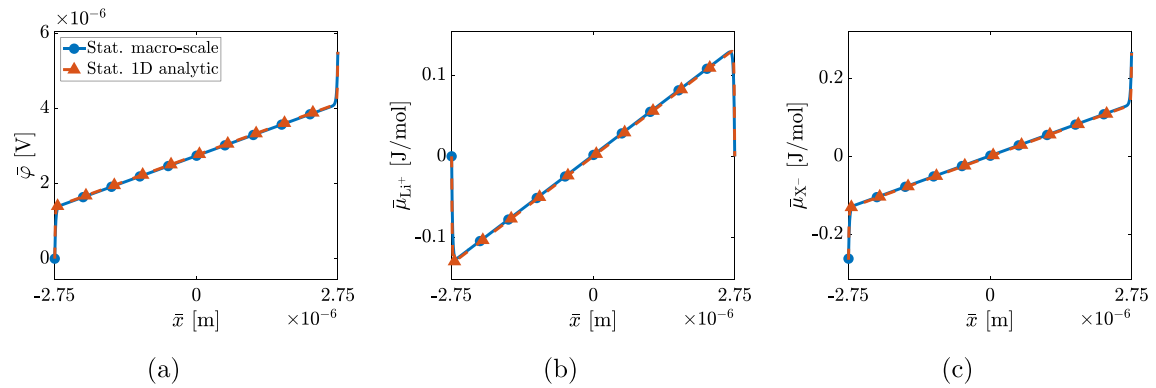

Fig. 8. Comparing macro-scale solution to 1D analytic solution at stationarity; (a) electric potential, (b) chemical potential of Li-ions and (c) chemical potential of X-ions.
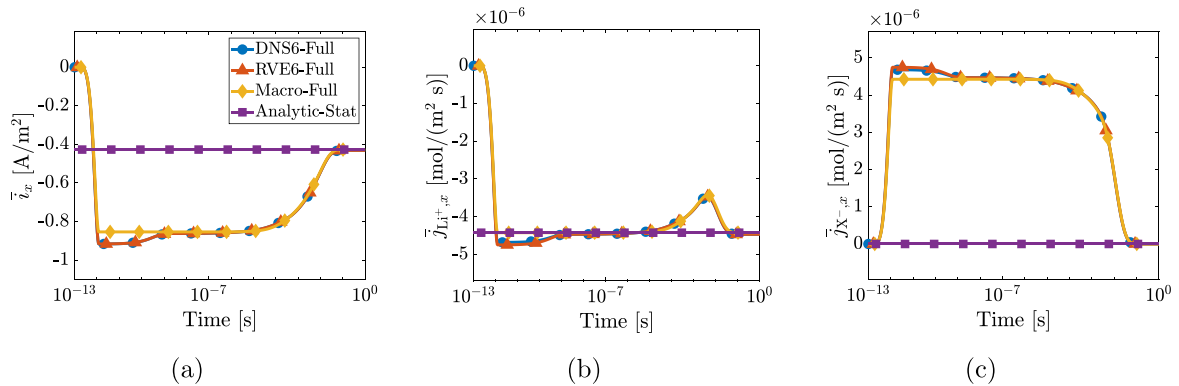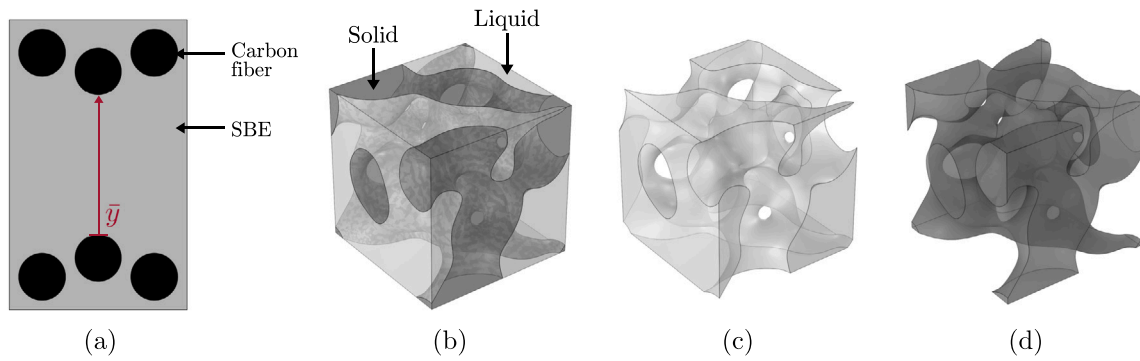

Fig. 9. Validation of fluxes from upscaled macro-scale problem based on (micro-stationary) 2D RVE; (a) current density, (b) ionic flux of Li-ions and (c) ionic flux of X-ions. Note that the purple curve is the analytical stationary flux, which validates the other transient fluxes at steady-state when $t \to \infty$.

Fig. 10. (a) 2D macro-scale domain, (b) full 3D RVE of SBE, (c) liquid electrolyte domain, and (d) solid polymer domain. Red line in (a) is used as a reference line for evaluation of spatial distributions. Size of macro-scale domain is 19×31 µm², while the RVE size is $500 \times 500 \times 500$ nm³.

Table 4
Outline of upscaled problem based on stationary 3D RVE.

(i)	Generate a bicontinuous 3D RVE
(ii)	Pre-compute effective coefficients for effective fluxes and storage terms according to the linear stationary 3D RVE problem (47)
(iii)	Consider a smooth macro-scale geometry in 2D that resembles the cross-section of a structural battery
(iv)	Apply conditions along fiber boundaries
(v)	Solve 2D macro-scale problem (21)

Table 5
Boundary conditions of the upscaled macro-scale problem based on 3D RVE.

Field	Top fibers	Bottom fibers	Left and right boundaries	Top and bottom boundaries
φ	$\varphi^{\mathrm{p}} = 0$	Positive ramp $\varphi^{\mathrm{p}}(t)$	Periodicity in φ	Zero flux condition
μ_{Li^+}	$\mu_{\mathrm{Li}^+}^{\mathrm{p}} = 0$	$\mu_{\mathrm{Li}^+}^{\mathrm{p}} = 0$	Periodicity in μ_{Li^+}	Zero flux condition
μ_{X^-}	Zero flux condition	Zero flux condition	Periodicity in μ_{X^-}	Zero flux condition

$$\varphi(x = L) \rightarrow \Delta\varphi, \tag{51b}$$

where the magnitude of the initial electric field after the ramp is identified as $\frac{\Delta\varphi}{2L}$, thus concluding that the magnitude reduction during charge accumulation at the boundaries corresponds to a factor of $1/2$, cf. Figs. 4(d) and 7(a).

As a last validation step, we compare the pre-computation based 2D macro-scale mid point solution to the DNS solution. Note that the homogenized RVE solution and the stationary 1D analytical solution are also included for reference, see Fig. 9. As expected, and as previously mentioned in Section 4.2, the agreement between the DNS and the macro-scale problem is good after $t = 10^{-9}$ s. This does not pose a problem if we consider all transport processes before $t = 10^{-9}$ s to be out of interest. The pre-computation based macro-scale problem is therefore a valid strategy in the considered application which consists of coupled problems with transport processes of various time scales, i.e. in the presence of time scale separation.

5.2. Upscaled macro-scale problem based on a 3D RVE

In this section, the goal is to provide a numerical example of a 2D macro-scale problem by using pre-computed upscaled coefficients based on a 3D RVE, see Fig. 10. The upscaled problem based on 3D RVE is demonstrated by following the steps outlined in Table 4.

The 3D RVE is generated using the same method as in Tu et al. (2020); it belongs to the microstructure class that is denoted as trabecular microstructures. Although the RVE is not fully representative, it is still an irregular microstructure that can be used to demonstrate the procedure of solving a 2D macro-scale problem with a non-trivial upscaling of a 3D RVE. For a discussion on RVE sizes and RVE representativeness, see e.g. Soyarslan et al. (2018). The geometric dimension of the macro-scale domain is 19x31 µm², while the RVE size is 500×500 nm². The macro-scale problem represents carbon fibers submerged in SBE. However, it is not a proper model of the structural battery due

to the lack of governing equations in the fiber domain and interface laws between the SBE and the carbon fibers that describe the electrochemical kinetics. Moreover, while the negative electrodes in a structural battery are simply the carbon fibers, the positive electrodes consist of carbon fibers coated with lithium metal oxide or olivine based particles, e.g. LiFePO₄, binder and conductive additives. To circumvent the modeling complexities pertaining to the structural battery, only the SBE is discretized here. Hence, the effects of the carbon fibers are taken into account via simplified boundary conditions as stated in Table 5. Therefore, this problem is solved solely for illustration purposes. The stationary 3D RVE problem is spatially discretized using 140 771 quadratic tetrahedral elements, resulting in a total of 394 097 degrees of freedom. The macro-scale problem is spatially discretized using 26 754 quadratic triangular elements, resulting in a total of 97 779 degrees of freedom. The time stepping is performed with a BDF2 scheme using 500 time steps with exponential spacing.

As expected, due to the similar choice of boundary conditions as in Section 4.1, the primary field distributions in Figs. 11(c)–11(e) are similar to the ones in Figs. 7(a)–7(c). However, unlike in Fig. 7(d), where the volume charge density has a skewed distribution, the corresponding quantity in Fig. 11(b) is anti-symmetrically distributed along the path between the carbon fibers in the center. This demonstrates that the observed skewness in Figs. 7(d)–7(f) is indeed a consequence of scale mixing effects stemming from the higher order storage terms in (24c) and (24g). In the limit of scale separation, this effect vanishes as $[\boldsymbol{x} - \bar{\boldsymbol{x}}] \rightarrow \boldsymbol{0}$. Although the length scale ratio between the macro-scale domain and the RVE is only roughly 30, it turns out to be sufficiently large for this problem.

Note that the current density in Fig. 11(a) is computed as $\bar{i} = \int_{\Gamma_{\mathrm{fib}}^-} \sum_{\alpha=1}^{2} z'_\alpha \boldsymbol{j}_\alpha \cdot \boldsymbol{n} \, \mathrm{d}\Gamma$, where Γ_{fib}^- corresponds to the bottom carbon fiber boundaries. For comparison, we also include $\bar{i}_{\mathrm{eff}} = \int_{\Gamma_{\mathrm{fib}}^-} \sum_{\alpha=1}^{2} z'_\alpha \boldsymbol{j}_{\alpha,\mathrm{eff}} \cdot \boldsymbol{n} \, \mathrm{d}\Gamma$ since it is the natural choice pertaining to the Neumann conditions defined in (27). Based on the comparison, it turns out that they coincide
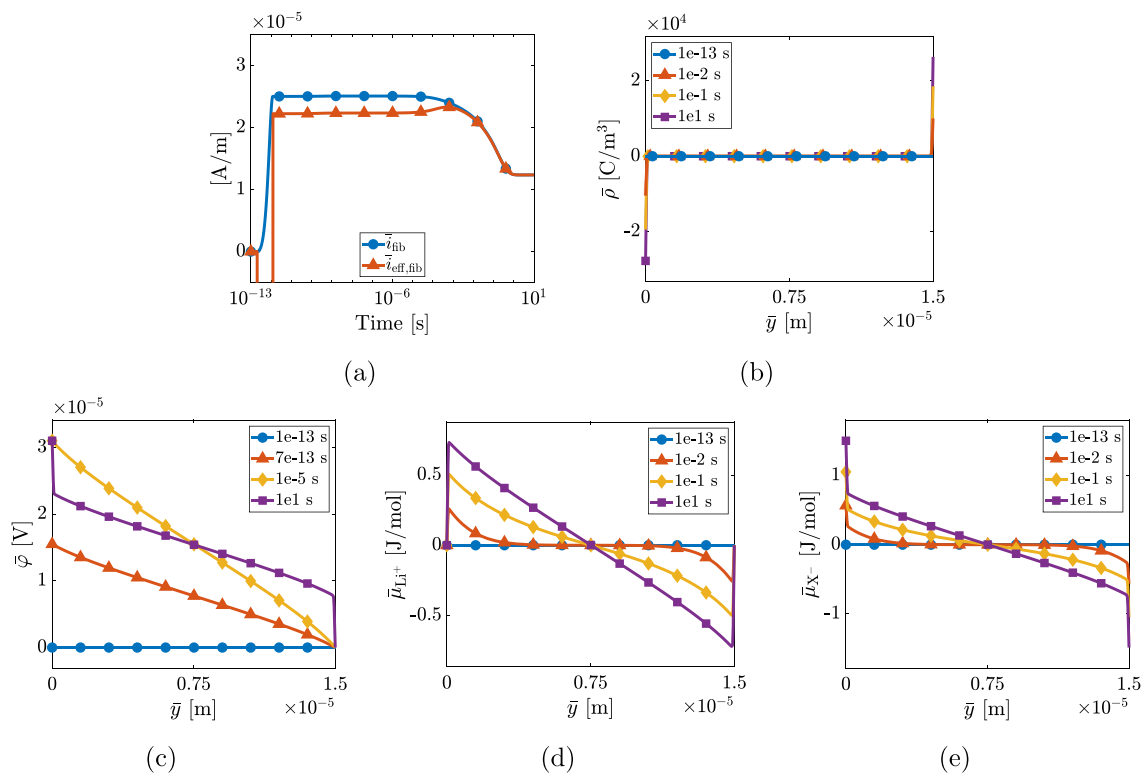
Fig. 11. (a) outgoing current density at the interface between the bottom carbon fibers and the SBE. Spatial distributions along the reference line defined in Fig. 10(a); (b) volume charge density, (c) electric potential, (d) chemical potential of Li-ions, and (e) chemical potential of X-ions.

already from $t = 10^{-3}$ s and onward. Between $t = 10^{-9}$ s and $t = 10^{-3}$ s, there is a small discrepancy between the current densities that will vanish in the limit of scale separation as seen in the higher order storage term in (24g). Although huge differences are observed during the ramping phase of the electric potential, these effects are neglected since such fast transport processes are out of interest. Moreover, the results in the initial time frame are also unreliable since micro-transient effects are neglected when solving the macro-scale problem based on pre-computations of the stationary RVE problem. Lastly, it should be noted that the fast loading rate clearly violates the assumption of electrostatics, which further motivates why the results during the ramping phase are considered to be out of interest.

6. Conclusions and outlook

We have shown that the theory of Variationally Consistent Homogenization (VCH) is applicable to electro-chemically coupled ion transport in a Structural Battery Electrolyte (SBE), which is modeled by coupling Gauss law (as opposed to using an electro-neutrality assumption) with a mass conservation law for each mobile species. In this paper, we have restricted the analysis to linear models. Based on this, we have also successfully derived the corresponding two scale model with proper scale bridging. In the Representative Volume Element (RVE) and validation study presented in Section 4, we evaluated the accuracy of the multi-scale approach by comparing the RVE results to a small subdomain of a 2D Direct Numerical Simulation (DNS) whose fine-scale features are defined by the RVE. In this validation step, we observed a clear agreement between the two simulations when subdomain DNS6 from the 2D DNS was used for validation. However, a small error between the two simulations was obtained when subdomain DNS3 from the 2D DNS was used instead. The reason for the error was most likely due to the small size of the 2D DNS, i.e., we had a poor separation of scales between the RVE problem and the DNS.

Another outcome from the RVE study was that the electrochemical problem gives rise to negligible transient effects due to the small time

scales related to the transport processes in the studied electrochemical system. This meant that the electrochemical problem possesses not only multiple length scales, but also multiple time scales. Based on this, we proposed replacing the fully transient RVE problem with its stationary counterpart in the upscaling procedure. Due to linearity, this resulted in an efficient solution scheme for the macro-scale problem since the upscaled constitutive fluxes from the RVE could be computed once and for all in an offline stage. The accuracy of this assumption was evaluated in Section 5.1 by comparing the blue curve (fully resolved DNS) to the yellow curve (micro-stationary two-scale model) in Fig. 9. The validation study showed that the micro-stationarity assumption is valid for transport processes that take place at larger time scales, in our example $\gtrsim 10^{-9}$ s.

Finally, the paper concluded with a numerical example of a 2D macro-scale problem using the proposed pre-computed upscaling on a 3D RVE, demonstrating the feasibility to solve larger problems efficiently.

As for future developments, the proposed two-scale model can be utilized as a component, e.g. in the full analysis of a structural battery. Regarding the model limitation, it would be of interest to consider non-linear effects, in particular related to the chemical potential. So far, a dilute solution assumption has been used, which gives rise to a linear (Fickian) diffusion law. The model could be enriched by e.g. accounting for direct interactions between the species, thus resulting in a non-linear diffusion model. Finally, for studying faster time-scales, which would be relevant for large microstructures, efficient methods for upscaling the transient RVE-response would be of great interest. One viable method would be to employ numerical model reduction, e.g. based on a snapshot-POD approach.

CRediT authorship contribution statement

Vinh Tu: Conceptualization, Methodology, Software, Formal analysis, Writing – original draft, Writing – review & editing, Visualization. **Fredrik Larsson:** Conceptualization, Methodology, Writing – review &

Table B.1

List of important symbols.

Symbol	Unit	Description
φ	[V]	Electric potential
μ_α	[J mol^{-1}]	Chemical potential
ρ	[C m^{-3}]	Volume charge density
$\boldsymbol{d}$	[C m^{-2}]	Electric displacement field/electric flux density
c_α	[mol m^{-3}]	Molar concentration
$\boldsymbol{j}_\alpha$	[mol m^{-2} s^{-1}]	Molar/ionic flux
$\boldsymbol{e}$	[V m^{-1}]	Electric field
z'_α	[C mol^{-1}]	Ionic charge
$\boldsymbol{i}$	[A m^{-2}]	Current density

Table B.2

Relevant physical constants.

Physical constant	Value	Unit	Description
ϵ_0	$8.8541878128 \cdot 10^{-12}$	[F m^{-1}]	Vacuum permittivity
F	96485.3329	[C mol^{-1}]	Faraday's constant
R	8.31446261815324	[J K^{-1} mol^{-1}]	Gas constant

editing, Supervision, Project administration, Funding acquisition. **Kenneth Runesson:** Conceptualization, Methodology, Writing – review & editing, Supervision, Project administration, Funding acquisition. **Ralf Jänicke:** Conceptualization, Methodology, Writing – review & editing, Supervision, Project administration, Funding acquisition.

Declaration of competing interest

Data availability

No data was used for the research described in the article.

Acknowledgments

Appendix A. Stationary sensitivity problems

In (46), it is shown that the stationary solution can be decomposed into a linear combination of sensitivity fields with time-dependent coefficients corresponding to macroscopic load histories. These sensitivity fields are given by the following stationary sensitivity problems:

(i) For the given sensitivity load $\bar{\varphi} = 1$, find the stationary sensitivity fields $\varphi_{\bar{\varphi}} \in \mathbb{P}_\square$, $\mu_{\alpha,\bar{\varphi}} \in \mathbb{M}_{\square,\alpha}$, $\lambda^{(\varphi)} \in \mathbb{T}_\square^{(\varphi)}$, $\lambda_\alpha^{(\mu)} \in \mathbb{T}_\square^{(\mu)}$, $\hat{\lambda}^{(\varphi)} \in \mathbb{R}$ and $\hat{\lambda}_\alpha^{(\mu)} \in \mathbb{R}$ that solve

$$\sum_{\alpha=1}^N m_{\square,\alpha}^{(\varphi)}(\mu_{\alpha,\bar{\varphi}}, \delta\varphi) - a_\square^{(\varphi)}(\varphi_{\bar{\varphi}}, \delta\varphi) - \left\langle\left\langle \lambda^{(\varphi)}[\![\delta\varphi]\!]_\square \right\rangle\right\rangle_\square$$
$$-\hat{\lambda}^{(\varphi)}\langle\delta\varphi\rangle_\square = 0 \quad \forall \delta\varphi \in \mathbb{P}_\square,$$
$$-\left\langle\left\langle \delta\lambda^{(\varphi)}[\![\varphi_{\bar{\varphi}}]\!]_\square \right\rangle\right\rangle_\square = 0 \quad \forall\delta\lambda^{(\varphi)} \in \mathbb{T}_\square^{(\varphi)},$$
$$-\left\langle \varphi_{\bar{\varphi}} \right\rangle_\square \delta\hat{\lambda}^{(\varphi)} = -\delta\hat{\lambda}^{(\varphi)} \quad \forall\delta\hat{\lambda}^{(\varphi)} \in \mathbb{R},$$

$$a_{\square,\alpha}^{(\mu)}(\mu_{\alpha,\bar{\varphi}}, \delta\mu_\alpha) + a_{\square,\alpha}^{(\mu\varphi)}(\varphi_{\bar{\varphi}}, \delta\mu_\alpha)$$
$$+\phi\left\langle\left\langle \lambda_\alpha^{(\mu)}[\![\delta\mu_\alpha]\!]_\square \right\rangle\right\rangle_{\square,\mathrm{E}} - \lambda_\alpha^{(\mu)}\phi\langle\delta\mu_\alpha\rangle_{\square,\mathrm{E}} = 0 \quad \forall\delta\mu_\alpha \in \mathbb{M}_{\square,\alpha},$$
$$\phi\left\langle\left\langle \delta\lambda_\alpha^{(\mu)}[\![\mu_{\alpha,\bar{\varphi}}]\!]_\square \right\rangle\right\rangle_{\square,\mathrm{E}} = 0 \quad \forall\delta\lambda_\alpha^{(\mu)} \in \mathbb{T}_\square^{(\mu)},$$
$$-\phi\left\langle \mu_{\alpha,\bar{\varphi}} \right\rangle_{\square,\mathrm{E}} \delta\hat{\lambda}_\alpha^{(\mu)} = 0 \quad \forall\delta\hat{\lambda}_\alpha^{(\mu)} \in \mathbb{R}.$$

Here, we identify the trivial solution $\varphi_{\bar{\varphi}} = 1$ and $\mu_{\alpha,\bar{\varphi}} = 0$ ($\lambda^{(\varphi)} = \lambda_\alpha^{(\mu)} = \hat{\lambda}^{(\varphi)} = \hat{\lambda}_\alpha^{(\mu)} = 0$). Hence, all pertinent fluxes and storage terms in (47) are invariant to $\bar{\varphi}$.

(ii) For the given sensitivity load $\boldsymbol{\nabla}\bar{\varphi} = \boldsymbol{e}_i$, find the stationary sensitivity fields $\varphi_{\bar{g}^\varphi(i)} \in \mathbb{P}_\square$, $\mu_{\alpha,\bar{g}^\varphi(i)} \in \mathbb{M}_{\square,\alpha}$, $\lambda^{(\varphi)} \in \mathbb{T}_\square^{(\varphi)}$, $\lambda_\alpha^{(\mu)} \in \mathbb{T}_\square^{(\mu)}$, $\hat{\lambda}^{(\varphi)} \in \mathbb{R}$ and $\hat{\lambda}_\alpha^{(\mu)} \in \mathbb{R}$ that solve

$$\sum_{\alpha=1}^N m_{\square,\alpha}^{(\varphi)}(\mu_{\alpha,\bar{g}^\varphi(i)}, \delta\varphi) - a_\square^{(\varphi)}(\varphi_{\bar{g}^\varphi(i)}, \delta\varphi) - \left\langle\left\langle \lambda^{(\varphi)}[\![\delta\varphi]\!]_\square \right\rangle\right\rangle_\square$$
$$-\hat{\lambda}^{(\varphi)}\langle\delta\varphi\rangle_\square = 0 \quad \forall\delta\varphi \in \mathbb{P}_\square,$$
$$-\left\langle\left\langle \delta\lambda^{(\varphi)}[\![\varphi_{\bar{g}^\varphi(i)}]\!]_\square \right\rangle\right\rangle_\square = -\left\langle\left\langle \delta\lambda^{(\varphi)}[\![\boldsymbol{x}]\!]_\square \right\rangle\right\rangle_\square \cdot \boldsymbol{e}_i \quad \forall\delta\lambda^{(\varphi)} \in \mathbb{T}_\square^{(\varphi)},$$
$$-\left\langle \varphi_{\bar{g}^\varphi(i)} \right\rangle_\square \delta\hat{\lambda}^{(\varphi)} = 0 \quad \forall\delta\hat{\lambda}^{(\varphi)} \in \mathbb{R},$$

$$a_{\square,\alpha}^{(\mu)}(\mu_{\alpha,\bar{g}^\varphi(i)}, \delta\mu_\alpha) + a_{\square,\alpha}^{(\mu\varphi)}(\varphi_{\bar{g}^\varphi(i)}, \delta\mu_\alpha)$$
$$+\phi\left\langle\left\langle \lambda_\alpha^{(\mu)}[\![\delta\mu_\alpha]\!]_\square \right\rangle\right\rangle_{\square,\mathrm{E}} - \lambda_\alpha^{(\mu)}\phi\langle\delta\mu_\alpha\rangle_{\square,\mathrm{E}} = 0 \quad \forall\delta\mu_\alpha \in \mathbb{M}_{\square,\alpha},$$
$$\phi\left\langle\left\langle \delta\lambda_\alpha^{(\mu)}[\![\mu_{\alpha,\bar{g}^\varphi(i)}]\!]_\square \right\rangle\right\rangle_{\square,\mathrm{E}} = 0 \quad \forall\delta\lambda_\alpha^{(\mu)} \in \mathbb{T}_\square^{(\mu)},$$
$$-\phi\left\langle \mu_{\alpha,\bar{g}^\varphi(i)} \right\rangle_{\square,\mathrm{E}} \delta\hat{\lambda}_\alpha^{(\mu)} = 0 \quad \forall\delta\hat{\lambda}_\alpha^{(\mu)} \in \mathbb{R}.$$

(iii) For the given sensitivity load $\bar{\mu}_\beta = 1$, find the stationary sensitivity fields $\varphi_{\bar{\mu}_\beta} \in \mathbb{P}_\square$, $\mu_{\alpha,\bar{\mu}_\beta} \in \mathbb{M}_{\square,\alpha}$, $\lambda^{(\varphi)} \in \mathbb{T}_\square^{(\varphi)}$, $\lambda_\alpha^{(\mu)} \in \mathbb{T}_\square^{(\mu)}$, $\hat{\lambda}^{(\varphi)} \in \mathbb{R}$ and $\hat{\lambda}_\alpha^{(\mu)} \in \mathbb{R}$ that solve

$$\sum_{\alpha=1}^N m_{\square,\alpha}^{(\varphi)}(\mu_{\alpha,\bar{\mu}_\beta}, \delta\varphi) - a_\square^{(\varphi)}(\varphi_{\bar{\mu}_\beta}, \delta\varphi) - \left\langle\left\langle \lambda^{(\varphi)}[\![\delta\varphi]\!]_\square \right\rangle\right\rangle_\square$$
$$-\hat{\lambda}^{(\varphi)}\langle\delta\varphi\rangle_\square = 0 \quad \forall\delta\varphi \in \mathbb{P}_\square,$$
$$-\left\langle\left\langle \delta\lambda^{(\varphi)}[\![\varphi_{\bar{\mu}_\beta}]\!]_\square \right\rangle\right\rangle_\square = 0 \quad \forall\delta\lambda^{(\varphi)} \in \mathbb{T}_\square^{(\varphi)},$$
$$-\left\langle \varphi_{\bar{\mu}_\beta} \right\rangle_\square \delta\hat{\lambda}^{(\varphi)} = 0 \quad \forall\delta\hat{\lambda}^{(\varphi)} \in \mathbb{R},$$

$$a_{\square,\alpha}^{(\mu)}(\mu_{\alpha,\bar{\mu}_\beta}, \delta\mu_\alpha) + a_{\square,\alpha}^{(\mu\varphi)}(\varphi_{\bar{\mu}_\beta}, \delta\mu_\alpha)$$
$$+\phi\left\langle\left\langle \lambda_\alpha^{(\mu)}[\![\delta\mu_\alpha]\!]_\square \right\rangle\right\rangle_{\square,\mathrm{E}} - \hat{\lambda}_\alpha^{(\mu)}\phi\langle\delta\mu_\alpha\rangle_{\square,\mathrm{E}} = 0 \quad \forall\delta\mu_\alpha \in \mathbb{M}_{\square,\alpha},$$
$$\phi\left\langle\left\langle \delta\lambda_\alpha^{(\mu)}[\![\mu_{\alpha,\bar{\mu}_\beta}]\!]_\square \right\rangle\right\rangle_{\square,\mathrm{E}} = 0 \quad \forall\delta\lambda_\alpha^{(\mu)} \in \mathbb{T}_\square^{(\mu)},$$
$$-\phi\left\langle \mu_{\alpha,\bar{\mu}_\beta} \right\rangle_{\square,\mathrm{E}} \delta\hat{\lambda}_\alpha^{(\mu)} = -\phi\,\delta\hat{\lambda}_\alpha^{(\mu)} \quad \forall\delta\hat{\lambda}_\alpha^{(\mu)} \in \mathbb{R}.$$

(iv) For the given sensitivity load $\boldsymbol{\nabla}\bar{\mu}_\beta = \boldsymbol{e}_i$, find the stationary sensitivity fields $\varphi_{\bar{g}_\beta^\mu(i)} \in \mathbb{P}_\square$, $\mu_{\alpha,\bar{g}_\beta^\mu(i)} \in \mathbb{M}_{\square,\alpha}$, $\lambda^{(\varphi)} \in \mathbb{T}_\square^{(\varphi)}$, $\lambda_\alpha^{(\mu)} \in \mathbb{T}_\square^{(\mu)}$, $\hat{\lambda}^{(\varphi)} \in \mathbb{R}$ and $\hat{\lambda}_\alpha^{(\mu)} \in \mathbb{R}$ that solve

$$\sum_{\alpha=1}^N m_{\square,\alpha}^{(\varphi)}(\mu_{\alpha,\bar{g}_\beta^\mu(i)}, \delta\varphi) - a_\square^{(\varphi)}(\varphi_{\bar{g}_\beta^\mu(i)}, \delta\varphi) - \left\langle\left\langle \lambda^{(\varphi)}[\![\delta\varphi]\!]_\square \right\rangle\right\rangle_\square$$
$$-\hat{\lambda}^{(\varphi)}\langle\delta\varphi\rangle_\square = 0 \quad \forall\delta\varphi \in \mathbb{P}_\square,$$
$$-\left\langle\left\langle \delta\lambda^{(\varphi)}[\![\varphi_{\bar{g}_\beta^\mu(i)}]\!]_\square \right\rangle\right\rangle_\square = 0 \quad \forall\delta\lambda^{(\varphi)} \in \mathbb{T}_\square^{(\varphi)},$$
$$-\left\langle \varphi_{\bar{g}_\beta^\mu(i)} \right\rangle_\square \delta\hat{\lambda}^{(\varphi)} = 0 \quad \forall\delta\hat{\lambda}^{(\varphi)} \in \mathbb{R},$$

$$a_{\square,\alpha}^{(\mu)}(\mu_{\alpha,\bar{g}_\beta^\mu(i)}, \delta\mu_\alpha) + a_{\square,\alpha}^{(\mu\varphi)}(\varphi_{\bar{g}_\beta^\mu(i)}, \delta\mu_\alpha)$$
$$+\phi\left\langle\left\langle \lambda_\alpha^{(\mu)}[\![\delta\mu_\alpha]\!]_\square \right\rangle\right\rangle_{\square,\mathrm{E}} - \hat{\lambda}_\alpha^{(\mu)}\phi\langle\delta\mu_\alpha\rangle_{\square,\mathrm{E}} = 0 \quad \forall\delta\mu_\alpha \in \mathbb{M}_{\square,\alpha},$$
$$\phi\left\langle\left\langle \delta\lambda_\alpha^{(\mu)}[\![\mu_{\alpha,\bar{g}_\beta^\mu(i)}]\!]_\square \right\rangle\right\rangle_{\square,\mathrm{E}}$$
$$= \phi\left\langle\left\langle \delta\lambda_\alpha^{(\mu)}[\![\boldsymbol{x}]\!]_\square \right\rangle\right\rangle_{\square,\mathrm{E}} \cdot \delta_{\alpha\beta}\,\boldsymbol{e}_i \quad \forall\delta\lambda_\alpha^{(\mu)} \in \mathbb{T}_\square^{(\mu)},$$
$$-\phi\left\langle \mu_{\alpha,\bar{g}_\beta^\mu(i)} \right\rangle_{\square,\mathrm{E}} \delta\hat{\lambda}_\alpha^{(\mu)} = (\delta_{\alpha\beta}\,\boldsymbol{e}_i \cdot [\bar{\boldsymbol{x}}_\mathrm{E} - \bar{\boldsymbol{x}}])\,\delta\hat{\lambda}_\alpha^{(\mu)} \quad \forall\delta\hat{\lambda}_\alpha^{(\mu)} \in \mathbb{R}.$$

Table B.3
Material parameters in liquid and solid phase.

Parameter	Value	Unit	Description	Reference
$c_{Li^+,0}$	1000	[mol m^{-3}]	Linearization concentration Li$^+$	Ihrner et al. (2017)
$c_{X^-,0}$	1000	[mol m^{-3}]	Linearization concentration X$^-$	Ihrner et al. (2017)
$\epsilon_{r,E}$	79.52	[-]	Relative permittivity (liquid electrolyte)	Estimated (Scrosati et al., 2013)
$\epsilon_{r,S}$	2	[-]	Relative permittivity (solid)	Estimated (Zha et al., 2021)
γ_{Li^+}	1	[m^3 mol^{-1}]	Activity coefficient Li$^+$	Assumed
γ_{X^-}	1	[m^3 mol^{-1}]	Activity coefficient X$^-$	Assumed
M_{Li^+}	$1.28 \cdot 10^{-10}$	[s mol^2 kg^{-1} m^{-3}]	Ionic mobility Li$^+$	Estimated (Dahbi et al., 2011)
M_{X^-}	$1.28 \cdot 10^{-10}$	[s mol^2 kg^{-1} m^{-3}]	Ionic mobility X$^-$	Estimated (Dahbi et al., 2011)
T	298.15	[K]	Temperature	Assumed
z_{Li^+}	1	[-]	Valence number Li$^+$	
z_{X^-}	-1	[-]	Valence number X$^-$	

As discussed in Section 3.4, we do not distinguish the notation of the Lagrange multipliers upon solving the stationary and the transient problem.

Appendix B. Symbols, material parameters and physical constants

See Tables B.1–B.3.

References

Asp, L.E., Greenhalgh, E.S., 2014. Structural power composites. Compos. Sci. Technol. 101, 41–61.

Asp, L.E., Johansson, M., Lindbergh, G., Xu, J., Zenkert, D., 2019. Structural battery composites: A review. Functional Compos. Struct. 1, 042001.

Bauer, G., Gravemeier, V., Wall, W.A., 2012. A stabilized finite element method for the numerical simulation of multi-ion transport in electrochemical systems. Comput. Methods Appl. Mech. Engrg. 223–224, 199–210.

Bharali, R., Larsson, F., Jänicke, R., 2021. Computational homogenisation of phase-field fracture. Eur. J. Mech. A Solids 88, 104247.

Carlstedt, D., Runesson, K., Larsson, F., Asp, L.E., 2022a. On the coupled thermo–electro–chemo–mechanical performance of structural batteries with emphasis on thermal effects. Eur. J. Mech. A Solids 94, 104586.

Carlstedt, D., Runesson, K., Larsson, F., Tu, V., Jänicke, R., Asp, L.E., 2022b. Computational modelling of structural batteries accounting for stress-assisted convection in the electrolyte. Int. J. Solids Struct. 238, 111343.

Carlstedt, D., Runesson, K., Larsson, F., Xu, J., Asp, L.E., 2020. Electro-chemo-mechanically coupled computational modelling of structural batteries. Multifunctional Mater. 3, 045002.

Costa, C.M., Lee, Y.-H., Kim, J.-H., Lee, S.-Y., Lanceros-Méndez, S., 2019. Recent advances on separator membranes for lithium-ion battery applications: From porous membranes to solid electrolytes. Energy Storage Mater. 22, 346–375.

Dahbi, M., Ghamouss, F., Tran-Van, F., Lemordant, D., Anouti, M., 2011. Comparative study of EC/DMC LiTFSI and LiPF6 electrolytes for electrochemical storage. J. Power Sources 196, 9743–9750.

Danilov, D., Notten, P., 2008. Mathematical modelling of ionic transport in the electrolyte of Li batteries. Electrochim. Acta 53, 5569–5578.

Dickinson, Edmund J.F., Limon-Petersen, Juan G., Compton, Richard G., 2011. The electroneutrality approximation in electrochemistry. J. Solid State Electrochem. 15, 1335–1345.

Doyle, M., Fuller, T.F., Newman, J., 1993. Modeling of galvanostatic charge and discharge of the lithium/polymer/insertion cell. J. Electrochem. Soc. 140, 1526–1533.

Doyle, M., Newman, J., 1995. The use of mathematical modeling in the design of lithium/polymer battery systems. Electrochim. Acta 40, 2191–2196, International symposium on polymer electrolytes.

Fredi, G., et al., 2018. Graphitic microstructure and performance of carbon fibre Li-ion structural battery electrodes. Multifunctional Mater. 1, 015003.

Griffiths, E., Wilmers, J., Bargmann, S., Reddy, B.D., 2020. Nanoporous metal based composites: Giving polymers strength and making metals move. J. Mech. Phys. Solids 137, 103848.

Hagberg, J., et al., 2018. Lithium iron phosphate coated carbon fiber electrodes for structural lithium ion batteries. Compos. Sci. Technol. 162, 235–243.

Hill, R., 1963. Elastic properties of reinforced solids: Some theoretical principles. J. Mech. Phys. Solids 11, 357–372.

Ihrner, N., Johannisson, W., Sieland, F., Zenkert, D., Johansson, M., 2017. Structural lithium ion battery electrolytes via reaction induced phase-separation. J. Mater. Chem. A 5, 25652–25659, 48.

Jänicke, R., Larsson, F., Runesson, K., 2020. A poro-viscoelastic substitute model of fine-scale poroelasticity obtained from homogenization and numerical model reduction. Comput. Mech. 65, 1063–1083.

Johannisson, W., Zenkert, D., Lindbergh, G., 2019. Model of a structural battery and its potential for system level mass savings. Multifunctional Mater. 2, 035002.

Kaessmair, S., Steinmann, P., 2018. Computational first-order homogenization in chemo-mechanics. Arch. Appl. Mech. 88, 271–286.

Kanno, R., Kawamoto, Y., Takeda, Y., Ohashi, S., Imanishi, N., Yamamoto, O., 1992. Carbon fiber as a negative electrode in lithium secondary cells. J. Electrochem. Soc. 139, 3397–3404.

Kjell, M.H., Jacques, E., Zenkert, D., Behm, M., Lindbergh, G., 2011. PAN-based carbon fiber negative electrodes for structural lithium-ion batteries. J. Electrochem. Soc. 158, A1455.

Larsson, F., Runesson, K., Saroukhani, S., Vafadari, R., 2011. Computational homogenization based on a weak format of micro-periodicity for RVE-problems. Comput. Methods Appl. Mech. Engrg. 200, 11–26.

Larsson, F., Runesson, K., Su, F., 2010. Variationally consistent computational homogenization of transient heat flow. Internat. J. Numer. Methods Engrg. 81, 1659–1686.

Moyer, K., Boucherbil, N.A., Zohair, M., Eaves-Rathert, J., Pint, C.L., 2020. Polymer reinforced carbon fiber interfaces for high energy density structural lithium-ion batteries. Sustain. Energy Fuels 4, 2661–2668.

Newman, J., Tiedemann, W., 1975. Porous-electrode theory with battery applications. AIChE J. 21, 25–41.

Öhman, M., Larsson, F., Runesson, K., 2013. Computational homogenization of liquid-phase sintering with seamless transition from macroscopic compressibility to incompressibility. Comput. Methods Appl. Mech. Engrg. 266, 219–228.

Polukhov, E., Keip, M.-A., 2020. Computational homogenization of transient chemo-mechanical processes based on a variational minimization principle. Adv. Model. Simul. Eng. Sci. 7, 35.

Salvadori, A., Bosco, E., Grazioli, D., 2014. A computational homogenization approach for Li-ion battery cells: Part 1 – formulation. J. Mech. Phys. Solids 65, 114–137.

Salvadori, A., Grazioli, D., Geers, M., 2015a. Governing equations for a two-scale analysis of Li-ion battery cells. Int. J. Solids Struct. 59, 90–109.

Salvadori, A., Grazioli, D., Geers, M., Danilov, D., Notten, P., 2015b. A multiscale-compatible approach in modeling ionic transport in the electrolyte of (lithium ion) batteries. J. Power Sources 293, 892–911.

Samson, E., Marchand, J., Robert, J.-L., Bournazel, J.-P., 1999. Modelling ion diffusion mechanisms in porous media. Internat. J. Numer. Methods Engrg. 46, 2043–2060.

Sanchez, J.S., Xu, J., Xia, Z., Sun, J., Asp, L.E., Palermo, V., 2021. Electrophoretic coating of LiFePO4/Graphene oxide on carbon fibers as cathode electrodes for structural lithium ion batteries. Compos. Sci. Technol. 208, 108768.

Sandstrom, C., Larsson, F., 2013. Variationally consistent homogenization of Stokes flow in porous media. Int. J. Multiscale Comput. Eng. 11.

Sandström, C., Larsson, F., Runesson, K., 2016. Homogenization of coupled flow and deformation in a porous material. Comput. Methods Appl. Mech. Engrg. 308, 535–551.

Schneider, L.M., Ihrner, N., Zenkert, D., Johansson, M., 2019. Bicontinuous electrolytes via thermally initiated polymerization for structural lithium ion batteries. ACS Appl. Energy Mater. 2, 4362–4369.

Scrosati, B., Abraham, K.M., Schalkwijk, W.V., Hassoun, J., 2013. Lithium Batteries - Advanced Technologies and Applications. John Wiley & Sons.

Shirshova, N., et al., 2013. Polymerised high internal phase ionic liquid-in-oil emulsions as potential separators for lithium ion batteries. J. Mater. Chem. A 1, 9612–9619, 34.

Soyarslan, C., Bargmann, S., Pradas, M., Weissmüller, J., 2018. 3D stochastic bicontinuous microstructures: Generation, topology and elasticity. Acta Mater. 149, 326–340.

Su, F., Larsson, F., Runesson, K., 2011. Computational homogenization of coupled consolidation problems in micro-heterogeneous porous media. Internat. J. Numer. Methods Engrg. 88, 1198–1218.

Tu, V., Asp, L.E., Shirshova, N., Larsson, F., Runesson, K., Jänicke, R., 2020. Performance of bicontinuous structural electrolytes. Multifunctional Mater. 3, 025001.

Wilmers, J., McBride, A., Bargmann, S., 2017. Interface elasticity effects in polymer-filled nanoporous metals. J. Mech. Phys. Solids 99, 163–177.

Xu, J., Lindbergh, G., Varna, J., 2018. Multiphysics modeling of mechanical and electrochemical phenomena in structural composites for energy storage: Single carbon fiber micro-battery. J. Reinf. Plast. Compos. 37, 701–715.

Zha, J.-W., Zheng, M.-S., Fan, B.-H., Dang, Z.-M., 2021. Polymer-based dielectrics with high permittivity for electric energy storage: A review. Nano Energy 89, 106438.